MDPI

Article

Fractal Structure Characteristics and Prospecting Direction of Dispersed Metals in the Eastern Guizhou Pb–Zn Metallogenic Belt, SW China

Zhongliang Cui [1], Jiaxi Zhou [2,3,]*, Kai Luo [2,3] and Maoda Lu [4]

[1] Jiangxi Institute of Applied Science and Technology, Nanchang 330100, China
[2] School of Earth Sciences, Yunnan University, Kunming 650500, China
[3] Key Laboratory of Critical Minerals Metallogeny in Universities of Yunnan Province, Kunming 650500, China
[4] 104 Geological Team, Guizhou Bureau of Geology and Mineral Exploration and Development, Duyu 558000, China
* Correspondence: zhoujiaxi@ynu.edu.cn

Abstract: The eastern Guizhou Pb–Zn metallogenic belt (EGMB) is an important source of Pb–Zn resources and other critical minerals (including dispersed metals, such as Ge, Cd and Ga) in China. In order to ensure the continuous resource supply of Pb–Zn and associated dispersed metals, it is urgent to explore the direction of further prospecting for them. Fractal theory can realize the fractal structure characterization of fault structures and the spatial distribution of mineral deposits, which is helpful for mineral exploration. However, the fault fractal research and prospecting application are still seldom covered in the EGMB. We used fractal theory to determine fine-scale fractal structure characteristics of fault structures and ore deposits in the EGMB, and Fry analysis to delineate favorable metallogenic areas. The results show that within a scale range of 3.670–58.716 km, the integrated faults capacity dimension (CPD) is 1.5095, the information dimension (IND) is 1.5391, and the correlation dimension (CRD) is 1.5436, indicating fault structures with high maturity, which are conducive to the migration and accumulation of ore-forming fluids. The multi-fractal spectrum width and height are 0.3203 and 1.5355, respectively, implying a significant metallogenic potential. The spatial distribution fractal dimensions (SDD) of Pb–Zn specifically and metal deposits in general are 1.0193 and 1.0709, respectively; the quantity distribution fractal dimensions (QDD) are 1.4225 and 1.4716, respectively, and the density distribution fractal dimensions (DDD) are 1.422 and 1.472, respectively, indicating strong clustering. Hence, the favorable metallogenic regions can be divided into four grades, among which grade I region is continuously distributed in space and has the greatest prospecting potential.

Keywords: fault structure; Pb–Zn deposits; dispersed metals; fractal structure characteristic; Fry analysis; prospecting direction; eastern Guizhou metallogenic belt; SW China

1. Introduction

The western Hubei–western Hunan–eastern Guizhou metallogenic belt is an important source of Pb–Zn metals in China [1,2]. Within this belt, the eastern Guizhou Pb–Zn metallogenic belt (EGMB) hosts a large number of Pb–Zn and other metal deposits/ore fields, including the Niujiaotang Cd-rich Pb–Zn ore field [2,3]. In recent years, many researchers have systematically studied the geological characteristics of the Pb–Zn deposits [4–8], a source of metallogenic materials [9–13] and ore-forming fluids [12,14–17], the ore genesis of deposits [2–4,6,12,17], and the metallogenic model [3,18–21]. These Pb–Zn deposits are obviously controlled by faults [2,12,22,23], and they belong to the Mississippi Valley-type (MVT) Pb–Zn deposits [2–4,12,14,24].

A previously developed fracture–lithology–fluid coupling metallogenic model has guided Pb–Zn exploration in this area and identified significant supernormal enrichment of Ge (more than 1000 times enrichment compared with the crustal abundance of Ge),

including large (e.g., Zhulingou) to super-large (e.g., Banbianjie) Ge-Zn deposits [21,25–30]. Dispersed elements are those that have very low abundance in the crust (mostly grades 10^{-9}) and are dispersed in rocks [31]. They are critical minerals that have great practical significance to national security and the development of emerging industries [32], especially in the development of "high-tech" technology and future energy [21,33]. Statistics show that: Ge, Cd, Ga, Tl, and other dispersed elements are enriched in Pb–Zn deposits and Pb–Zn poly-metallic deposits [34], and mainly exist in the form of symbiotic associations [34–39]; and MVT Pb–Zn deposits are enriched with one or more dispersed elements compared with other types of Pb–Zn deposits or Pb–Zn poly-metallic deposits [2,31,38,40–46]. In summary, the huge metallogenic potential of the EGMB offers a potential production base for scarce resource minerals (e.g., Pb–Zn) and critical minerals (dispersed metals) in China. To ensure the continuous resource supply, it is of great theoretical and practical significance to strengthen research on the metallogenic law of dispersed metals, and to explore potential directions for future prospecting.

Although there have been many research achievements in the EGMB, so far, the fault fractal research and prospecting application are seldom covered. Fractal theory, which was proposed by the famous mathematician, Mandelbrot [47], can reveal the inner connection between the part and the whole of things; it can describe complex structures in detail and quantitatively reveal the hidden laws [48]. Fractal theory has been applied in the quantitative characterization of faults [49–54], the spatial distribution of deposits [48,55–59], metallogenic laws, and prospecting prediction [51,60–70]. Currently, three basic conclusions are generally recognized in the study of fault fractal [55]: (1) the fault system has fractal characteristics; (2) the fractal dimension of the fault structure is related to the connectivity of the fault (geological body); and (3) the fractal dimension of the fault structure is closely related to geological mineralization, which can be used as an indicator of metallogenic prediction. However, in the coupling study of fault fractal and deposit distribution, there are few reports on the research results of deposit spatial location prediction, which needs further exploration.

In this study, we applied fractal theory to quantitatively describe the coupling relationship between the fractal structure of faults of the EGMB and the spatial distribution of ore deposits. In addition, we performed Fry analysis of the ore deposits. Based on the results, we identified favorable prospecting directions for the exploration of Pb–Zn and associated critical minerals (dispersed metals).

2. Geological Background

The EGMB is located on the southeastern margin of the Yangtze block, and extends from the Bamianshan intra-continental deformation belt to the northwest to the Xuefengshan structural belt to the southeast (Figure 1a) [3]. Magmatic activity in the EGMB is not obvious [12,23], and magmatic rocks (e.g., potassium–magnesium lamprophyre) are sporadic (Figure 1b). The EGMB may have experienced varies periods of orogeny, including those during the Caledonian, Hercynian, Indosinian–Yanshanian, and other periods [23,71–73], and folds and fault structures are widely developed. Fault structures are mainly NE-trending (including NNE-trending), but are NW-trending and near-NS-trending in part. The basement is Neoproterozoic shallow metamorphic rocks. In the sedimentary cover, except for the Upper Paleozoic Carboniferous and the Mesozoic-Cenozoic Jurassic, Paleogene, and Neogene missing, the others are exposed. Among them, Cambrian carbonate strata are widely exposed and are the most important ore-bearing horizon [3,12,23]. Ore deposits in the EGMB are obviously controlled by faults (especially NE-trending fault structures) [3,12,22,23]. Of the 61 metal deposits, all are medium-low temperature hydrothermal deposits, including 53 Pb–Zn deposits, 5 Sb deposits, and 3 Hg deposits. From the perspectives of ore-bearing horizon, main ore-controlling factors, and genesis types of deposits, the deposits in the area are highly similar. As such, the study area has the prerequisites for quantitatively exploring the coupling relationship between fault structures and deposit distribution.
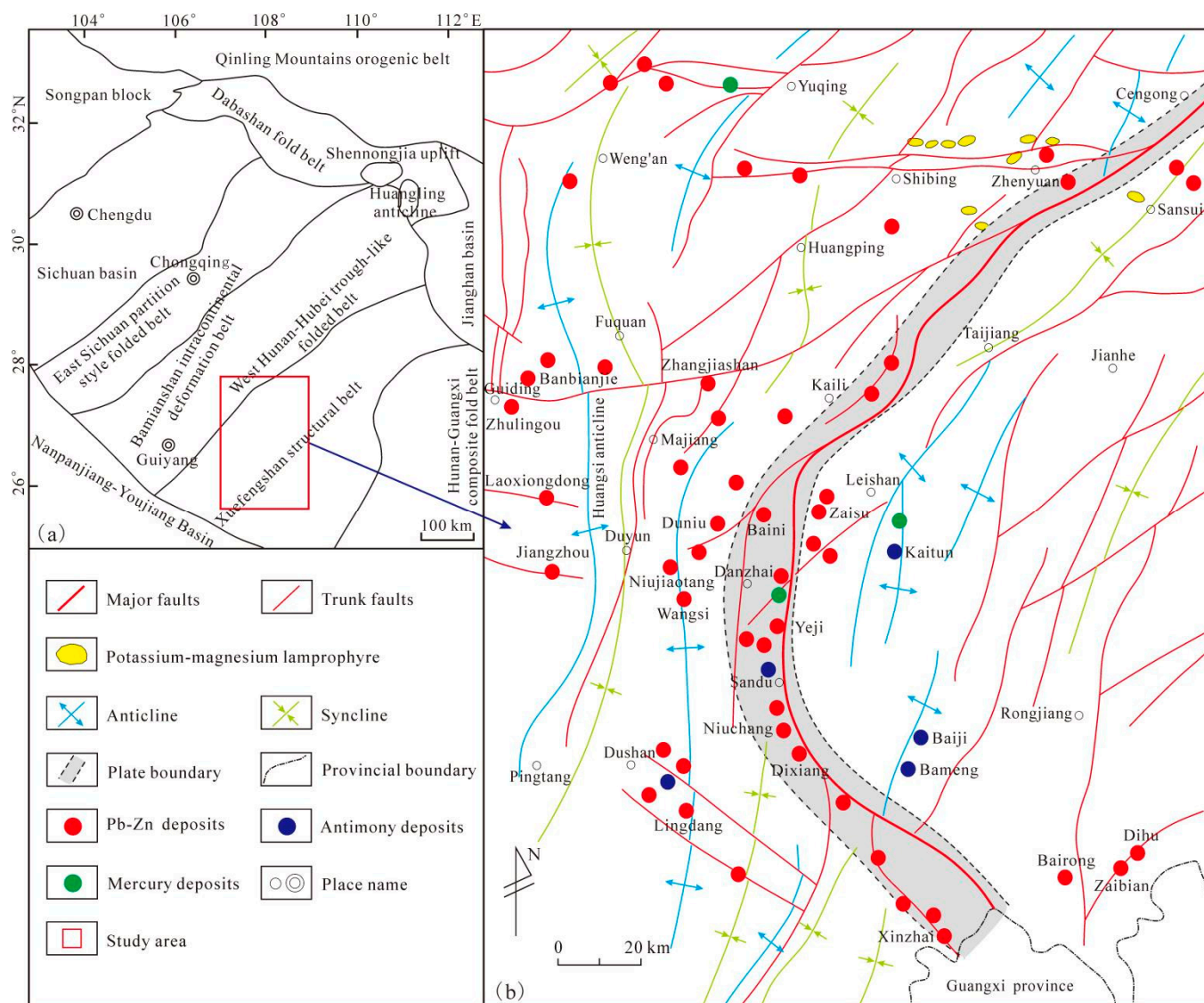
Figure 1. Geotectonic position of the study area: (**a**) according to Ref. [3] and fault structures, deposits distribution map (**b**): according to Ref. [26].

3. Single Fractal Characteristics of Fault Structures

3.1. Calculation Method

3.1.1. Capacity Dimension, D_0 Calculation

At present, there are many calculation methods for the capacity dimension of linear structures, including the box-counting dimension method, the circle covering method, and the length-frequency statistics method [74–76]. Among them, the box-counting dimension method is intuitive and easy to understand, and offers accurate statistics and strong operability. Therefore, we adopted the box-counting dimension method for the calculation of the capacity dimension (CPD) based on the fault structures and ore-deposit distribution map (Figure 1b). The algorithm was as follows: square grids with different side lengths r (r = L, L/2, L/4, and L/8 . . . , which are proportional sequences with a common ratio equal to 0.5) were used to cover the study area and the number of grids $N(r)$ covering the faults was calculated. If $N(r)$ and r satisfied the following power-law relationship (Equation (1)), the research object was fractal:

$$N(r) = Cr^{-D_0} \tag{1}$$

where C is a constant and D_0 is the CPD value that attempted to acquire. Taking the logarithm of Equation (1) yields Equation (2), from which the CPD value D_0 was obtained by taking the absolute value of the slope of the straight line:

$$\ln N(r) = -D_0 \ln r + \ln c \tag{2}$$

The specific steps of the calculation process were as follows: (1) two-dimensional orthogonal grids with side lengths of 58.716, 29.358, 14.679, 7.340, and 3.670 km were used to cover the study area. Then, the numbers of grids $N(r)$ covered by integrated faults, NE-trending faults, NW-trending faults, near-SN-trending faults, near-EW-trending faults, major faults, and the plate contact transition zone were counted. In Excel, we took ln$r$ as the horizontal axis and ln$N(r)$ as the vertical axis, and drew a straight regression line to obtain CPD values of different types of faults; (2) numbering the two-dimensional orthogonal grid with a side length of 58.716 km, the study area was divided into 12 divisions (Figure 2). For each division, the number $N(r)$ of different two-dimensional orthogonal grids covering faults with side lengths of 29.358, 14.679, 7.340, and 3.670 km were counted. Use Excel, we drew a straight regression line to obtain the CPD value of the overall faults of the division; and (3) numbering the two-dimensional orthogonal grid with a side length of 29.358 km, the study area was divided into 48 subdivisions (Figure 2). For each subdivision, the numbers $N(r)$ of different two-dimensional orthogonal grids covering faults with side lengths of 14.679, 7.340, and 3.670 km were counted. Using Excel, we drew a regression fitting line to obtain the overall CPD value of faults within the subdivision.

3.1.2. Information Dimension, D_1 Calculation

The fault information dimension (IND) not only considers whether a two-dimensional grid is crossed by faults, but also considers the number (or probability) of crossing faults. The study area was covered by a two-dimensional orthogonal grid with side length r, and it was assumed that faults were divided into $N(r)$ parts. If faults appeared in the i-th orthogonal grid, the probability was $P_i(r)$ (Equation (3)) and the total amount of information at this time was $I(r)$ (Equation (4)).

$$P_i(r) = \frac{n_i}{\sum\limits_{i=1}^{N(r)} n_i} \tag{3}$$

$$I(r) = -\sum_{i=1}^{N(r)} P_i(r) \ln P_i(r) \tag{4}$$

After transforming the side length r of the two-dimensional orthogonal grid, if there is the following linear relationship between $I(r)$ and ln$r$ (Equation (5)), the IND value, D_1, can be obtained from the slope of the straight line:

$$I(r) = -D_1 \ln r + I_0 \tag{5}$$

The specific steps of the calculation process were as follows: (1) two-dimensional orthogonal grids with side lengths of 58.716, 29.358, 14.679, 7.340, and 3.670 km were used to cover the study area. Then, the information contents $I(r)$ of integrated faults, NE-trending faults, NW-trending faults, near-SN-trending faults, near-EW-trending faults, and major faults were calculated. In Excel, we took ln$r$ as the horizontal axis and $I(r)$ as the vertical axis, and drew a straight regression line to obtain the IND values of different types of faults; (2) for each division (Figure 2), the overall information content $I(r)$ of the faults was calculated when the two-dimensional orthogonal grids with side lengths of 29.358, 14.679, 7.340, and 3.670 km were covered. We used Excel to draw a straight regression line to obtain the overall IND value of the faults in the division; and (3) for each subdivision (Figure 2), the overall information content $I(r)$ of the faults was calculated when covered by two-dimensional

orthogonal grids with side lengths of 14.679, 7.340, and 3.670 km. We used Excel to draw a regression fitting line to obtain the overall IND value of faults in the subdivision.
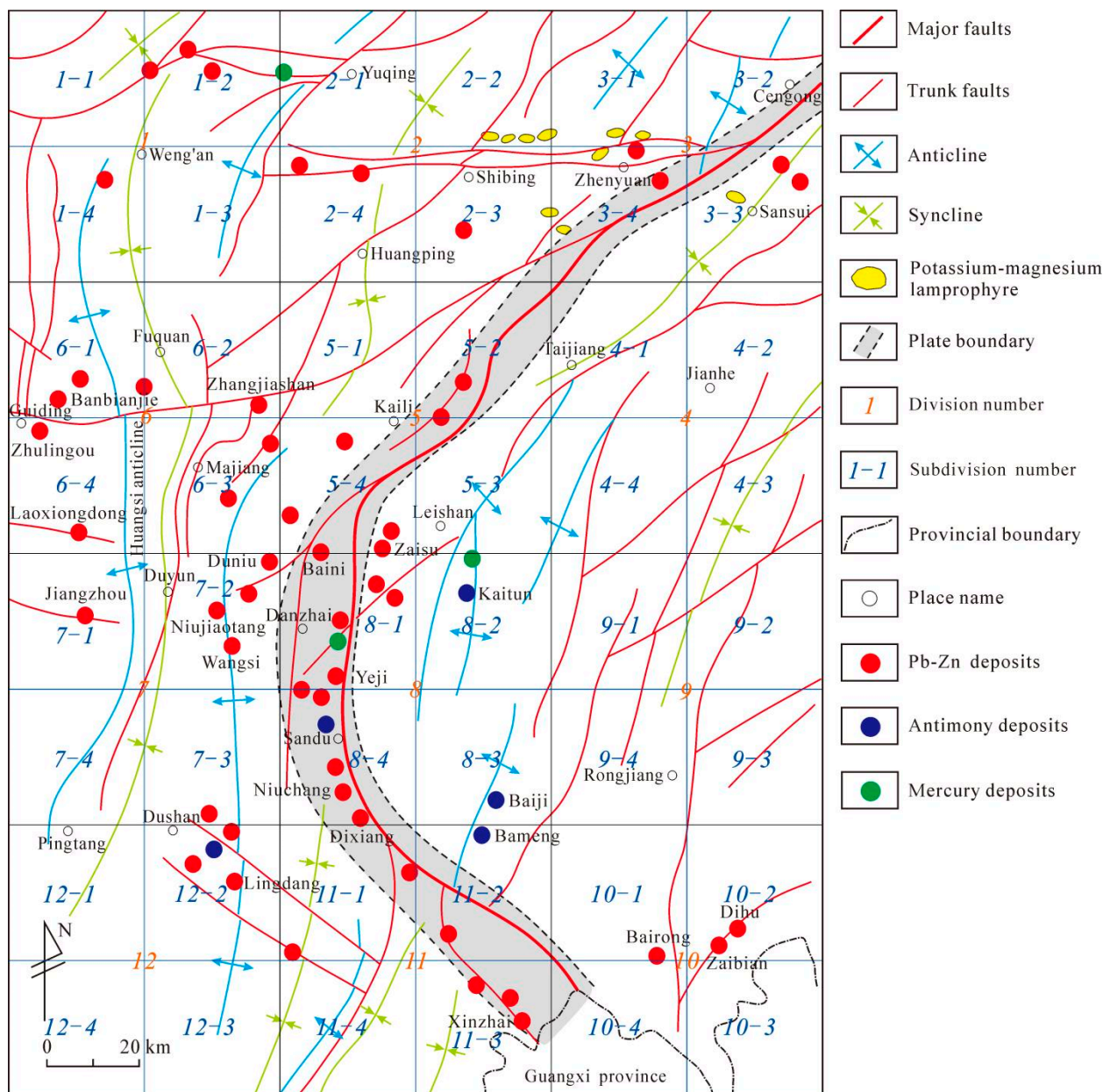
Figure 2. Computation partition map of fractal dimension (modified from Ref. [26]).

3.1.3. Correlation Dimension, D$_2$ Calculation

The calculation process for the correlation dimension (CRD) values was similar to that of the IND, and followed Equation (6):

$$I(r) = -\ln \sum_{i=1}^{N(r)} P_i^2(r) \tag{6}$$

3.2. Single Fractal Characteristics of Faults across the Whole Area

Statistical parameters of fault fractal dimension values are listed in Table 1; ln*r* versus ln*N*(*r*) plots for integrated faults, NW-trending faults, NE-trending faults, near-SN-trending

faults, near-EW-trending faults, major faults, and the plate contact transition zone with their linear regression parameters are shown in Figures 3–5.

Table 1. Statistical table of calculation parameters of fractal dimensions for fault structures in the eastern Guizhou Pb–Zn metallogenic belt (EGMB).

Category	CPD, D_0				IND, D_1			CRD, D_2		
	r (km)	$N(r)$	$\ln r$	$\ln N(r)$	r (km)	$\ln r$	$I(r)$	r (km)	$\ln r$	$I(r)$
Integrated faults	58.716	12	4.073	2.485	58.716	4.073	2.366	58.716	4.073	2.291
	29.358	45	3.380	3.807	29.358	3.380	3.692	29.358	3.380	3.606
	14.679	146	2.686	4.984	14.679	2.686	4.874	14.679	2.686	4.767
	7.340	368	1.993	5.908	7.340	1.993	5.836	7.340	1.993	5.743
	3.670	785	1.300	6.666	3.670	1.300	6.628	3.670	1.300	6.572
NE-trending faults	58.716	11	4.073	2.398	58.716	4.073	2.257	58.716	4.073	2.165
	29.358	37	3.380	3.611	29.358	3.380	3.475	29.358	3.380	3.369
	14.679	114	2.686	4.736	14.679	2.686	4.628	14.679	2.686	4.518
	7.340	281	1.993	5.638	7.340	1.993	5.582	7.340	1.993	5.509
	3.670	570	1.300	6.346	3.670	1.300	6.316	3.670	1.300	6.275
NW-trending faults	58.716	6	4.073	1.792	58.716	4.073	1.676	58.716	4.073	1.569
	29.358	11	3.380	2.398	29.358	3.380	2.307	29.358	3.380	2.213
	14.679	25	2.686	3.219	14.679	2.686	3.170	14.679	2.686	3.114
	7.340	53	1.993	3.970	7.340	1.993	3.957	7.340	1.993	3.937
	3.670	95	1.300	4.554	3.670	1.300	4.550	3.670	1.300	4.544
Near-SN-trending faults	58.716	4	4.073	1.386	58.716	4.073	1.273	58.716	4.073	1.176
	29.358	6	3.380	1.792	29.358	3.380	1.676	29.358	3.380	1.569
	14.679	13	2.686	2.565	14.679	2.686	2.479	14.679	2.686	2.392
	7.340	30	1.993	3.401	7.340	1.993	3.370	7.340	1.993	3.329
	3.670	64	1.300	4.159	3.670	1.300	4.122	3.670	1.300	4.040
Near-EW-trending faults	58.716	4	4.073	1.386	58.716	4.073	1.311	58.716	4.073	1.259
	29.358	10	3.380	2.303	29.358	3.380	2.211	29.358	3.380	2.120
	14.679	18	2.686	2.890	14.679	2.686	2.834	14.679	2.686	2.774
	7.340	34	1.993	3.526	7.340	1.993	3.469	7.340	1.993	3.409
	3.670	71	1.300	4.263	3.670	1.300	4.248	3.670	1.300	4.226
Major faults	58.716	6	4.073	1.792	58.716	4.073	1.792	58.716	4.073	1.792
	29.358	13	3.380	2.565	29.358	3.380	2.565	29.358	3.380	2.565
	14.679	25	2.686	3.219	14.679	2.686	3.219	14.679	2.686	3.219
	7.340	51	1.993	3.932	7.340	1.993	3.932	7.340	1.993	3.932
	3.670	100	1.300	4.605	3.670	1.300	4.605	3.670	1.300	4.605
Plate contact transition zone	58.716	8	4.073	2.079						
	29.358	17	3.380	2.833			-			
	14.679	43	2.686	3.761						
	7.340	112	1.993	4.718						
	3.670	328	1.300	5.793						

From Figures 3–5: (1) the coefficient of determination (degree of fitting) R^2 of the 19 regression lines range from 0.9854 to 0.9994, with most >0.99. The overall fitting degree of the straight lines is relatively high, showing that the fault structures have good statistical self-similarity on scales 3.670–58.716 km; (2) the integrated faults, NE-trending faults, NW-trending faults, near-SN-trending faults, near-EW-trending faults, and major fault CPD values are 1.5095, 1.4316, 1.0239, 1.0322, 1.0065, and 1.0090, respectively; the IND values are 1.5391, 1.4752, 1.0673, 1.0665, 1.0290, and 1.0090, respectively; and the CRD values are 1.5436, 1.4947, 1.1072, 1.0803, 1.0421, and 1.0090, respectively. The CPD value of the plate contact transition zone is 1.3435; (3) CPD values decrease as follows: integrated faults > NE-trending faults > plate contact transition zone > near-SN-trending faults > NW-trending faults > major faults > near-EW-trending faults. IND and CRD values decrease as follows: integrated faults > NE-trending faults > NW-trending faults > near-SN-trending faults > near-EW-trending faults > major faults; (4) based on the CPD, IND, and CRD, the fractal dimension value of integrated faults is the largest, closely followed by that of NE-trending faults; this reflects

the dominance of NE-trending faults in the EGMB and is consistent with regional tectonic characteristics; and (5) only one major fault was involved in the calculation of the fractal dimension, and so the values of the CPD, IND, and CRD were equal; however, we believe that major faults are still of great significance to the mineralization of the study area.

Figure 3. Linear fitting diagrams of the capacity dimension (CPD) calculation for faults in the eastern Guizhou Pb–Zn metallogenic belt (EGMB). The ln*r* versus ln*N*(*r*) plots of CPD data for (**a**) Integrated faults; (**b**) NE-trending faults; (**c**) NW-trending faults; (**d**) Near-SN-trending faults; (**e**) Near-EW-trending faults; (**f**) Major faults; and (**g**) Plate contact transition zone, showing their linear regression parameters.
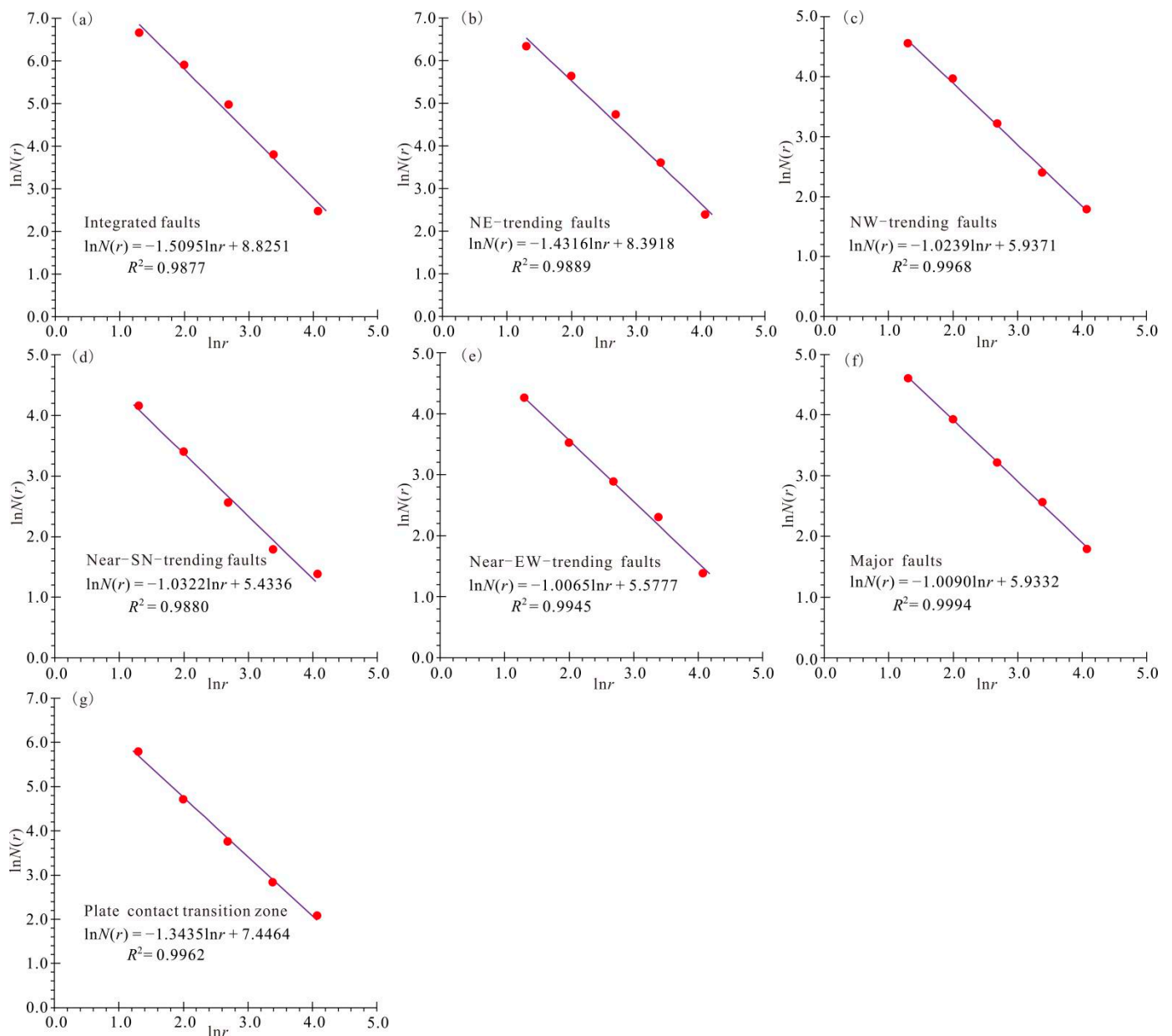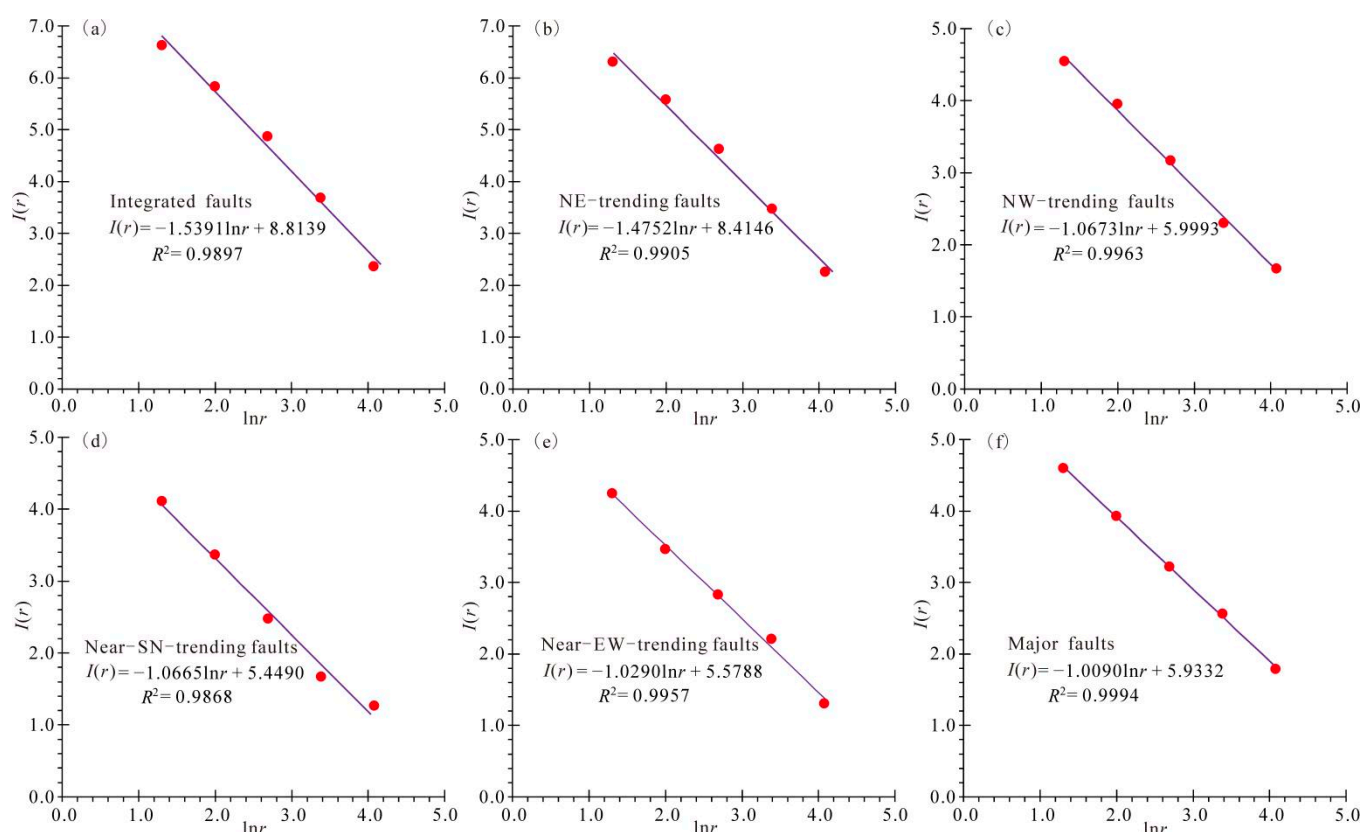
Figure 4. Linear fitting diagrams of the information dimension (IND) calculation for faults in the eastern Guizhou Pb–Zn metallogenic belt (EGMB). The $\ln r$ versus $I(r)$ plots of IND data for (**a**) Integrated faults; (**b**) NE-trending faults; (**c**) NW-trending faults; (**d**) Near-SN-trending faults; (**e**) Near-EW-trending faults; and (**f**) Major faults, showing their linear regression parameters.

The fractal dimension value of a fault structure is related to the connectivity of the fault (geological body). That is to say, with an increasing fractal dimension value of the fault structure, the spatial distribution of the fault structure becomes increasingly complex, the permeability of the fault (geological body) becomes stronger, and the connectivity improves. Therefore, an increasing fractal dimension value is more conducive to the activation of ore-forming elements and the migration and accumulation of ore-forming fluids. Based on the critical fractal dimension of faults (1.22–1.38) [77], the CPD values of integrated faults, NE-trending faults, and the plate contact transition zone are 1.5095, 1.4316, and 1.3435, respectively; the values for NW-trending faults, near-SN-trending faults, and near-EW-trending faults are all <1.22. Based on these results, we concluded that the overall metallogenic geological conditions of the EGMB are good. In particular, the plate contact transition zone is conducive to ore formation, which is consistent with the belt-like distribution of ore deposits along this zone.

The fault CPD of the EGMB is larger than those of most areas in China (Table 2), including ore fields, metallogenic belts, and ore concentration areas, and is close to the upper limit of the active area (Diwa area) CPD in mainland China. Among regions with smaller fractal scales (upper limit) than the EGMB, the fault CPD of the EGMB is larger than that of the Zhaoyuan gold ore concentration area, but smaller than those of the southeastern Guangxi gold and silver mineralization area, the Qitianling ore concentration area of southern Hunan, and the Yadu–Mangdong metallogenic belt of northwest Guizhou Province. Among regions with the same fractal scales (upper limit) as the EGMB, the fault CPD of the EGMB is larger than that of the Kangguertage gold belt in east Tianshan, but smaller than those of Xikuangshan–Longshan, Dashenshan, and Simingshan Sb belts in central Hunan Province. Among regions with larger fractal scales (upper limit) than the

EGMB, the fault CPD of the EGMB is larger than those of Southern China and Sichuan Province, but is close to those of Pb–Zn ore concentration regions bordering the three provinces of Sichuan, Yunnan, and Guizhou.
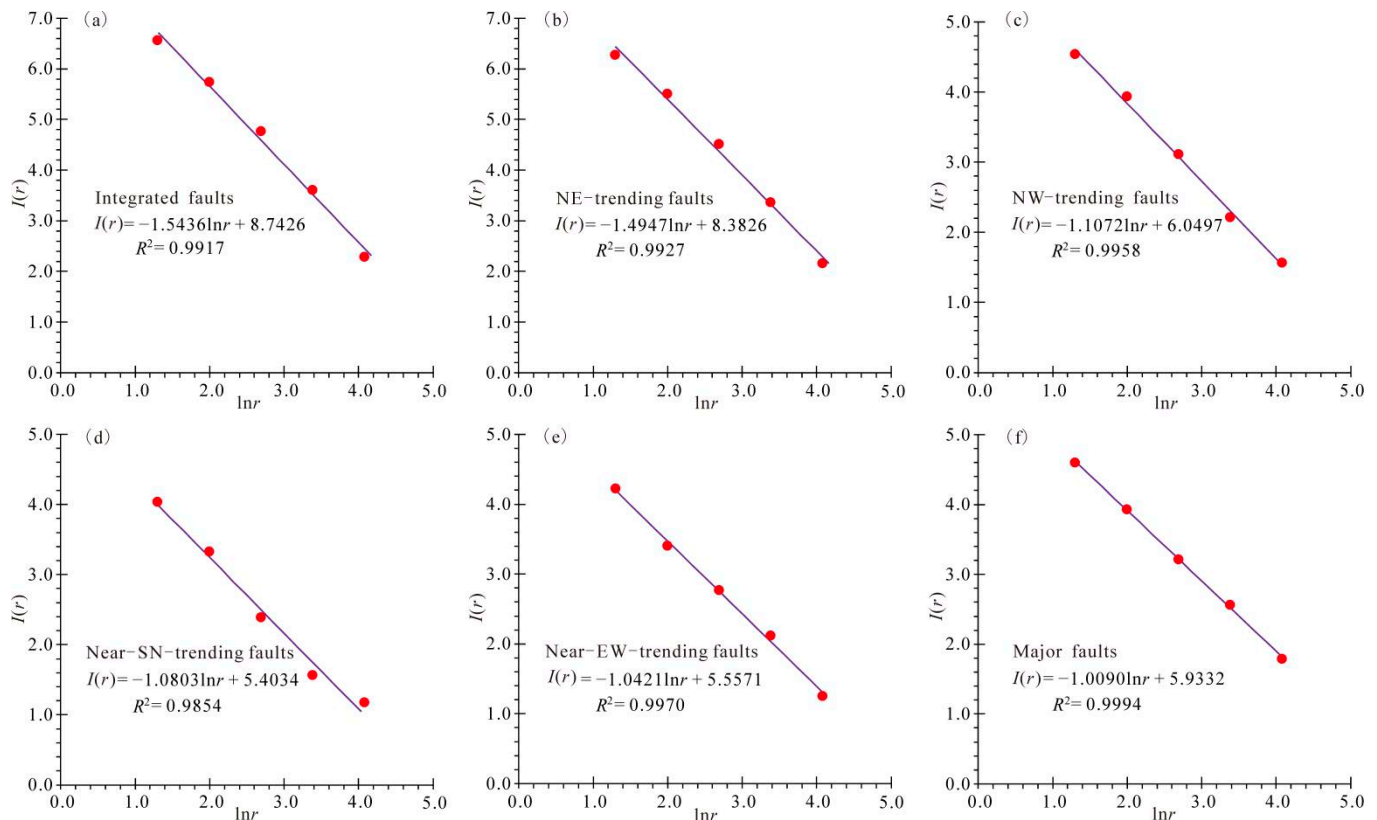

Figure 5. Linear fitting diagrams for the correlation dimension (CRD) calculation of faults in the eastern Guizhou Pb–Zn metallogenic belt (EGMB). The ln$r$ versus $I(r)$ plots of CRD data for (**a**) Integrated faults; (**b**) NE-trending faults; (**c**) NW-trending faults; (**d**) Near-SN-trending faults; (**e**) Near-EW-trending faults; and (**f**) Major faults, showing their linear regression parameters.

Table 2. Statistical table of fractal dimension for fault structures in some areas of China.

Region	Scale Interval (km)	CPD, D_0	IND, D_1	CRD, D_2	Reference
Activity Area of Continent in China (Diwa Area)	8–256	1.236–1.624	-	-	
Stable Area of Continent in China (platform area)	8–256	0.827–1.074	-	-	[49]
Yungui Activity Area	8–256	1.332	-	-	
China Continent	8–256	1.493	-	-	
Shell Binding Site	8–256	>1.5	-	-	
Sichuan-Yunnan-Guizhou Pb–Zn Metallogenic Province	9.336–149.373	1.5395	-	-	[54]
Zhaxikang Ore Concentration Area	0.073–4.7	1.249	-	-	[75]
Gudui–Longzi Region, Tibet	1.875–30	1.678	-	-	[78]
Tongling Ore Concentration Area	0.1–3	1.29	-	-	[52]
Jiaojia District, Jiaodong	0.50–16.00	1.3507	-	-	
Sanshandao-Cangshang Gold Mine Field in Jiaojia District	0.25–4.00	1.0103	-	-	[79]

Table 2. *Cont.*

Region	Scale Interval (km)	CPD, D_0	IND, D_1	CRD, D_2	Reference
Jiaojia Gold Mine Field in Jiaojia District	0.25–4.00	1.3198	-	-	
Canzhuang-Lingshangou Gold Mine Field in Jiaojia District	0.25–4.00	1.3656	-	-	
Xiyou–Zhuqiao Area in Jiaojia District (Mineral-free Area)	0.25–4.00	1.1315	-	-	
Kangguertage Gold Belt in East Tianshan	1.69412–54.2118	0.716	-	-	[48]
South China	25–400	1.4142	-	-	[80]
Jiangnan Diwa Region in South China	10–160	1.5939	-	-	[81]
Southeast Diwa Region in South China	10–160	1.6800	-	-	
Xikuangshan–Longshan Sb Ore Belt in Central Hunan	5–60	1.8183	1.8102	-	
Simingshan Sb Ore Belt in Central Hunan	5–60	1.7346	1.7067	-	[82]
Damshenshan Sb Ore Belt in Central Hunan	5–60	1.5975	1.5933	-	
Zhaoyuan Gold Ore Concentration Area	1–5	1.4806	-	-	[51]
Gold and Silver Metallogenic Area in Southeast Guangxi	1.25–40	1.61	-	-	[83]
Qitianling Ore Concentration Area in Southern Hunan	0.625–10	1.656	-	-	[84]
Hutouya Polymetallic Ore Collection Area, Qinghai Province	0.15–0.7	1.085	-	-	[85]
Gejiu Mining Area in Southeast Yunnan	0.5–5	1.432	-	-	
Malage Ore Field	0.5–5	1.093	-	-	[86]
Laochang Ore Field	0.5–5	1.263	-	-	
Kafang Ore Field	0.5–5	1.121	-	-	
Southern Jiangxi Province	0.5–10	1.2797	-	-	[87]
Faults of Maokou Formation in Southeast Sichuan	2.5–40	1.423	1.467	1.468	[50]
Xiciwa Area in Bozhong Sag	0.5–8	1.2137	1.2903	1.3582	[88]
Sichuan Area	3.75–120	1.4524	1.5136	1.5455	[89]
Shuiyanba Ore Field, Hezhou, Guangxi Province	0.171875–5.5	1.3475	-	-	[90]
Yadu-Mangdong Metallogenic Belt in NW Guizhou Province	3.371–26.965	1.6052	1.6051	-	[91]
EGMB	3.670–58.716	1.5095	1.5391	1.5436	this article

The IND and CRD of faults in China are less well studied than the CPD. From the limited data available, IND and CRD of fault structures in the EGMB are larger than those in areas with smaller fractal scales (upper limit), including the Maokou Formation in southeastern Sichuan and Xiciwa in the Bozhong sag. Among regions with larger fractal scales (upper limit) than the EGMB, the fractal dimension values are similar (e.g., the Sichuan area). Finally, among regions with similar fractal scales (upper limit) compared to the EGMB, the IND of fault structures in the EGMB is smaller than those of the Xikuangshan–Longshan, Dashenshan, and Simingshan Sb belts of Central Hunan.

3.3. Single Fractal Characteristics of Fault Divisions

The coefficient of determination of the straight line fitted by the division's fractal dimension values is 0.9648–0.9983 (Tables 3–5), and the straight line has a high degree of fit, indicating that fault structures within the divisions have good statistical self-similarity. The CPD values of the divisions range from 0.9230 to 1.5095 (Table 3), and the median is 1.4003. The IND values of the divisions range from 0.9746 to 1.5262 (Table 4), and the median is 1.4164. The CRD values of the divisions range from 1.0222 to 1.5410 (Table 5), and the median is 1.4195. Pb–Zn deposits are developed in 10 of the 12 divisions, and the fractal dimension value (CPD, IND, CRD) interval of the developed Pb–Zn deposit area covers the

fractal dimension values (CPD, IND, CRD) of all divisions. Therefore, in order to explore the coupling relationship between fractal dimension values and ore deposit distribution, subdivisions were divided on the basis of divisions (Figure 2), and the fractal dimension values of subdivisions were calculated.

Table 3. Statistical table of division for the capacity dimension (CPD) calculation parameters.

Division Number	Fractal Scale, r (km)				CPD, D_0	Coefficient of Determination (R^2)
	29.358	14.679	7.340	3.670		
1	4	12	34	68	1.3765	0.9901
2	4	14	36	92	1.4934	0.9946
3	4	15	42	91	1.5009	0.9863
4	4	15	35	76	1.3967	0.9827
5	4	14	43	90	1.5095	0.9875
$N(r)$　6	4	14	33	77	1.4038	0.9899
7	4	9	18	30	0.9721	0.9901
8	4	11	25	50	1.2116	0.9928
9	4	16	41	93	1.4976	0.9843
10	4	8	14	28	0.9230	0.9983
11	4	14	36	71	1.3812	0.9823
12	1	4	11	19	1.4204	0.9648

Table 4. Statistical table of division for the information dimension (IND) calculation parameters.

Division Number	Fractal Scale, r (km)				IND Values, D_1	Coefficient of Determination (R^2)
	29.358	14.679	7.340	3.670		
1	1.309	2.415	3.481	4.188	1.4001	0.9905
2	1.339	2.563	3.496	4.472	1.4907	0.9961
3	1.362	2.622	3.685	4.480	1.5028	0.9901
4	1.334	2.636	3.498	4.299	1.4077	0.9855
5	1.382	2.575	3.694	4.461	1.4943	0.9909
$I(r)$　6	1.305	2.487	3.403	4.279	1.4192	0.9947
7	1.277	2.164	2.871	3.379	1.0119	0.9856
8	1.288	2.322	3.166	3.892	1.2486	0.9936
9	1.310	2.651	3.650	4.503	1.5262	0.9891
10	1.242	2.043	2.599	3.309	0.9746	0.9956
11	1.295	2.582	3.545	4.240	1.4135	0.9820
12	0.000	1.332	2.398	2.944	1.4282	0.9689

Table 5. Statistical table of division for the correlation dimension (CRD) calculation parameters.

Division Number	Fractal Scale, r (km)				CRD Values, D_2	Coefficient of Determination (R^2)
	29.358	14.679	7.340	3.670		
1	1.232	2.354	3.427	4.146	1.4161	0.9907
2	1.294	2.498	3.406	4.408	1.4791	0.9966
3	1.339	2.546	3.626	4.440	1.4980	0.9927
4	1.289	2.572	3.420	4.249	1.4035	0.9875
5	1.378	2.526	3.620	4.406	1.4686	0.9931
$I(r)$　6	1.241	2.358	3.301	4.192	1.4131	0.9972
7	1.184	2.120	2.844	3.348	1.0412	0.9823
8	1.185	2.254	3.107	3.863	1.2822	0.9936
9	1.242	2.537	3.573	4.457	1.5410	0.9925
10	1.099	1.997	2.549	3.276	1.0222	0.9918
11	1.240	2.534	3.495	4.207	1.4228	0.9828
12	0.000	1.273	2.398	2.944	1.4367	0.9723

3.4. Single Fractal Characteristics of Fault Subdivisions

The subdivisions were squares with sides of 29.358 km, and so a reasonable upper limit of the study scale was 29.358 km. To ensure that fault structures can be regarded as an ideal straight line or curve shape to the greatest extent, theoretically speaking, the lower limit of the research scale should be as large as possible. Taking into account the control scale of the fault structure on the deposit space, the research scale interval used in the calculation of the fractal dimension value of the subdivisions was 3.670–29.358 km. However, considering the calculation characteristics of the CPD, IND, and CRD, a scale interval of 3.670–29.358 km was used for the calculation of the subdivision CPD, and a scale interval of 3.670–14.679 km was used for the calculation of IND and CPD. The statistics of the calculation parameters of the fractal dimension value of the subdivisions are shown in Tables 6 and 7. The subdivision CPD values are 0 to 1.6834, with a median of 1.3712. The subdivision IND values are 0 to 1.6091, with a median of 1.1797. The subdivision CRD values are 0 to 1.6179, with a median of 1.2010.

Table 6. Statistical table of subdivision for the capacity dimension (CPD) calculation parameters.

Sub-Division Number/Serial Number	Fractal Scale, r (km)				CPD Values, D_0	Coefficient of Determination (R^2)
	29.358	**14.679**	**7.340**	**3.670**		
1-1/1	1	4	10	19	1.4066	0.9713
1-2/2	1	4	11	23	1.5031	0.9809
1-3/11	1	2	5	10	1.1288	0.9968
1-4/12	1	2	8	16	1.4001	0.9800
2-1/3	1	3	9	22	1.4964	0.9977
2-2/4	1	4	9	20	1.4136	0.9792
2-3/9	1	3	9	27	1.5850	1.0000
2-4/10	1	4	9	23	1.4741	0.9859
3-1/5	1	3	11	20	1.4841	0.9808
3-2/6	1	4	9	20	1.4136	0.9792
3-3/7	1	4	9	18	1.3680	0.9718
3-4/8	1	4	13	33	1.6834	0.9925
4-1/17	1	4	9	18	1.3680	0.9718
4-2/18	1	4	8	15	1.2721	0.9597
4-3/19	1	4	11	26	1.5561	0.9878
4-4/20	1	3	7	17	1.3485	0.9965
5-1/15	1	4	12	27	1.5850	0.9865
5-2/16	1	4	15	31	1.6770	0.9821
5-3/21	1	3	8	14	1.2838	0.9809
5-4/22	1	3	8	18	1.3925	0.9955
6-1/13	1	3	8	21	1.4593	0.9990
6-2/14	1	4	10	23	1.4893	0.9845
6-3/23	1	3	10	21	1.4914	0.9911
6-4/24	1	4	5	12	1.1077	0.9276
7-1/25	1	3	5	8	0.9737	0.9524
7-2/26	1	3	7	11	1.1601	0.9684
7-3/35	1	1	1	2	0.3000	0.6000
7-4/36	1	2	5	9	1.0832	0.9937
8-1/27	1	4	12	29	1.6160	0.9899
8-2/28	1	2	2	2	0.3000	0.6000
8-3/33	1	2	3	4	0.6585	0.9608
8-4/34	1	3	8	15	1.3136	0.9862

Note: The "$N(r)$" label appears in the Sub-Division Number/Serial Number column spanning the table.

Table 6. *Cont.*

Sub-Division Number/Serial Number	Fractal Scale, *r* (km)				CPD Values, D_0	Coefficient of Determination (R^2)
	29.358	14.679	7.340	3.670		
9-1/29	1	4	13	33	1.6834	0.9925
9-2/30	1	4	8	19	1.3744	0.9773
9-3/31	1	4	12	27	1.5850	0.9865
9-4/32	1	4	8	14	1.2423	0.9521
10-1/41	1	2	4	9	1.0510	0.9984
10-2/42	1	3	6	9	1.0510	0.9565
10-3/43	1	1	1	3	0.4755	0.6000
10-4/44	1	2	3	7	0.9007	0.9836
11-1/39	1	4	11	23	1.5031	0.9809
11-2/40	1	4	12	22	1.4964	0.9721
11-3/45	1	3	5	10	1.0703	0.9749
11-4/46	1	3	8	16	1.3416	0.9903
12-1/37	0	0	0	0	0.0000	-
12-2/38	1	4	11	19	1.4204	0.9648
12-3/47	0	0	0	0	0.0000	-
12-4/48	0	0	0	0	0.0000	-

Table 7. Statistical table of calculation parameters for the information dimension (IND) and correlation dimension (CRD) of subdivision.

Subdivision Number/Serial Number	*r* (km)	ln*r*	*I(r)* for IND	IND, D_1	R^2	*I(r)* for CRD	CRD, D_2	R^2
1-1/1	14.679	2.686	1.332			1.273		
	7.340	1.993	2.272	1.1501	0.9894	2.231	1.1740	0.9896
	3.670	1.300	2.926			2.900		
1-2/2	14.679	2.686	1.321			1.269		
	7.340	1.993	2.338	1.2723	0.9922	2.281	1.2684	0.9924
	3.670	1.300	3.085			3.027		
1-3/11	14.679	2.686	0.637			0.588		
	7.340	1.993	1.561	1.1797	0.9944	1.504	1.1853	0.9956
	3.670	1.300	2.272			2.231		
1-4/12	14.679	2.686	0.693			0.693		
	7.340	1.993	2.079	1.5001	0.9643	2.079	1.5001	0.9643
	3.670	1.300	2.773			2.773		
2-1/3	14.679	2.686	1.079			1.059		
	7.340	1.993	2.133	1.4111	0.9980	2.079	1.3828	0.9986
	3.670	1.300	3.035			2.976		
2-2/4	14.679	2.686	1.277			1.184		
	7.340	1.993	2.254	1.2274	0.9927	2.197	1.2767	0.9930
	3.670	1.300	2.979			2.954		
2-3/9	14.679	2.686	0.995			0.898		
	7.340	1.993	2.079	1.6091	0.9997	1.962	1.6179	0.9991
	3.670	1.300	3.226			3.141		
2-4/10	14.679	2.686	1.352			1.327		
	7.340	1.993	2.023	1.2669	0.9818	1.974	1.2578	0.9784
	3.670	1.300	3.108			3.070		
3-1/5	14.679	2.686	1.055			1.022		
	7.340	1.993	2.272	1.3876	0.9771	2.231	1.3936	0.9793
	3.670	1.300	2.979			2.954		

Table 7. *Cont.*

Subdivision Number/Serial Number	r (km)	ln r	I(r) for IND	IND, D$_1$	R^2	I(r) for CRD	CRD, D$_2$	R^2
3-2/6	14.679 7.340 3.670	2.686 1.993 1.300	1.330 2.272 2.965	1.1797	0.9923	1.281 2.231 2.924	1.1853	0.9919
3-3/7	14.679 7.340 3.670	2.686 1.993 1.300	1.332 2.146 2.857	1.1001	0.9985	1.273 2.088 2.813	1.1112	0.9989
3-4/8	14.679 7.340 3.670	2.686 1.993 1.300	1.311 2.505 3.461	1.5512	0.9959	1.259 2.449 3.415	1.5555	0.9964
4-1/17	14.679 7.340 3.670	2.686 1.993 1.300	1.330 2.164 2.890	1.1259	0.9984	1.281 2.120 2.890	1.1610	0.9994
4-2/18	14.679 7.340 3.670	2.686 1.993 1.300	1.330 2.043 2.686	0.9784	0.9991	1.281 1.997 2.655	0.9911	0.9994
4-3/19	14.679 7.340 3.670	2.686 1.993 1.300	1.369 2.303 3.194	1.3162	0.9998	1.350 2.197 3.107	1.2674	0.9996
4-4/20	14.679 7.340 3.670	2.686 1.993 1.300	1.099 1.946 2.833	1.2513	0.9998	1.099 1.946 2.833	1.2513	0.9998
5-1/15	14.679 7.340 3.670	2.686 1.993 1.300	1.321 2.393 3.245	1.3881	0.9956	1.269 2.287 3.165	1.3680	0.9982
5-2/16	14.679 7.340 3.670	2.686 1.993 1.300	1.373 2.649 3.404	1.4651	0.9785	1.362 2.590 3.364	1.4442	0.9831
5-3/21	14.679 7.340 3.670	2.686 1.993 1.300	1.040 2.043 2.639	1.1537	0.9788	0.981 1.997 2.639	1.1962	0.9834
5-4/22	14.679 7.340 3.670	2.686 1.993 1.300	1.079 1.850 2.839	1.2696	0.9950	1.059 2.297 2.781	1.2424	0.9400
6-1/13	14.679 7.340 3.670	2.686 1.993 1.300	0.974 1.951 2.968	1.4385	0.9999	0.901 1.834 2.878	1.4264	0.9990
6-2/14	14.679 7.340 3.670	2.686 1.993 1.300	1.215 2.098 3.066	1.3353	0.9993	1.099 1.994 2.976	1.3540	0.9993
6-3/23	14.679 7.340 3.670	2.686 1.993 1.300	1.099 2.243 2.997	1.3695	0.9861	1.099 2.187 2.941	1.3292	0.9891
6-4/24	14.679 7.340 3.670	2.686 1.993 1.300	1.386 1.792 2.485	0.7925	0.9777	1.386 1.792 2.485	0.7925	0.9777
7-1/25	14.679 7.340 3.670	2.686 1.993 1.300	1.099 1.609 2.079	0.7076	0.9994	1.099 1.609 2.079	0.7076	0.9994

Table 7. *Cont.*

Subdivision Number/Serial Number	r (km)	ln$r$	$I(r)$ for IND	IND, D_1	R^2	$I(r)$ for CRD	CRD, D_2	R^2
7-2/26	14.679 7.340 3.670	2.686 1.993 1.300	1.040 1.906 2.369	0.9592	0.9703	0.981 1.856 2.331	0.9738	0.9714
7-3/35	14.679 7.340 3.670	2.686 1.993 1.300	0.000 0.000 0.693	0.5000	0.7500	0.000 0.000 0.693	0.5000	0.7500
7-4/36	14.679 7.340 3.670	2.686 1.993 1.300	0.693 1.609 2.197	1.0850	0.9843	0.693 1.609 2.197	1.0850	0.9843
8-1/27	14.679 7.340 3.670	2.686 1.993 1.300	1.369 2.428 3.336	1.4188	0.9980	1.350 2.380 3.294	1.4023	0.9988
8-2/28	14.679 7.340 3.670	2.686 1.993 1.300	0.693 0.693 0.693	<0.5	-	0.693 0.693 0.693	<0.5	-
8-3/33	14.679 7.340 3.670	2.686 1.993 1.300	0.693 1.099 1.386	0.5000	0.9905	0.693 1.099 1.386	0.5000	0.9905
8-4/34	14.679 7.340 3.670	2.686 1.993 1.300	1.055 2.079 2.708	1.1925	0.9812	1.022 2.079 2.708	1.2165	0.9789
9-1/29	14.679 7.340 3.670	2.686 1.993 1.300	1.358 2.479 3.320	1.4154	0.9932	1.332 2.392 3.477	1.5472	1.0000
9-2/30	14.679 7.340 3.670	2.686 1.993 1.300	1.330 2.025 2.912	1.1418	0.9951	1.281 1.966 2.870	1.1464	0.9937
9-3/31	14.679 7.340 3.670	2.686 1.993 1.300	1.352 2.441 3.283	1.3929	0.9945	1.327 2.388 3.263	1.3968	0.9970
9-4/32	14.679 7.340 3.670	2.686 1.993 1.300	1.386 2.079 2.639	0.9037	0.9962	1.386 2.079 2.639	0.9037	0.9962
10-1/41	14.679 7.340 3.670	2.686 1.993 1.300	0.693 1.386 2.197	1.0850	0.9980	0.693 1.386 2.197	1.0850	0.9980
10-2/42	14.679 7.340 3.670	2.686 1.993 1.300	1.099 1.792 2.197	0.7925	0.9776	1.099 1.792 2.197	0.7925	0.9776
10-3/43	14.679 7.340 3.670	2.686 1.993 1.300	0.000 0.000 1.099	0.7925	0.7500	0.000 0.000 1.099	0.7925	0.7500
10-4/44	14.679 7.340 3.670	2.686 1.993 1.300	0.637 1.055 1.889	0.9036	0.9646	0.588 1.022 1.829	0.8958	0.9707
11-1/39	14.679 7.340 3.670	2.686 1.993 1.300	1.352 2.352 3.108	1.2669	0.9936	1.327 2.297 3.070	1.2578	0.9958

Table 7. *Cont.*

Subdivision Number/Serial Number	r (km)	ln r	I(r) for IND	IND, D_1	R^2	I(r) for CRD	CRD, D_2	R^2
11-2/40	14.679	2.686	1.352			1.327		
	7.340	1.993	2.441	1.2341	0.9757	2.388	1.2242	0.9795
	3.670	1.300	3.063			3.024		
11-3/45	14.679	2.686	1.099			1.099		
	7.340	1.993	1.609	0.8685	0.9924	1.609	0.8685	0.9924
	3.670	1.300	2.303			2.303		
11-4/46	14.679	2.686	1.040			0.981		
	7.340	1.993	2.043	1.2350	0.9902	1.997	1.2560	0.9908
	3.670	1.300	2.752			2.722		
12-1/37	14.679	2.686	0.000			0.000		
	7.340	1.993	0.000	0.0000	-	0.000	0.0000	-
	3.670	1.300	0.000			0.000		
12-2/38	14.679	2.686	1.332			1.273		
	7.340	1.993	2.398	1.1631	0.9666	2.398	1.2058	0.9616
	3.670	1.300	2.944			2.944		
12-3/47	14.679	2.686	0.000			0.000		
	7.340	1.993	0.000	0.0000	-	0.000	0.0000	-
	3.670	1.300	0.000			0.000		
12-4/48	14.679	2.686	0.000			0.000		
	7.340	1.993	0.000	0.0000	-	0.000	0.0000	-
	3.670	1.300	0.000			0.000		

The determination coefficient R^2 value of the fitting straight line in the calculation of fractal dimension value was small for a small number of subdivisions (e.g., subdivision 10-3). In addition, the slope of the fitted straight line in the calculation of fractal dimension value for a small number of partitions was zero, and only the value range could be judged (e.g., the IND and CRD of subdivision 8-2). However, these phenomena had little effect on the coupling relationship between the fractal dimensions of subdivisions and the spatial distribution of deposit.

The main reasons are as follows: (1) among the 48 capacity-dimensional data in the subdivisions, only three have determination coefficients R^2 of <0.9; (2) compared with other data, the size relationship of such data is still very reliable. For example, the calculated value of the CPD of subdivision 10-3 is 0.4755, which is larger than the calculated values of subdivisions 7-3, 8-2, 12-1, 12-3, and 12-4, but is smaller than the calculated values of other subdivisions. This result is consistent with the original meaning of the capacity-dimensional representation. The CPD, also known as the box dimension, was originally used to characterize the ability of a fractal to occupy a box under the corresponding research scale. The larger the fractal dimension value, the stronger the ability to occupy the box. The relationship between the calculated CPD value of subdivision 10-3 and those of other subdivisions is consistent with the original meaning of the representation of the capacity dimension; and (3) the value of such data is relatively low in the overall data, and has no effect on the judgment of the favorable fractal dimension interval of the coupling relationship between fractal dimension value and the spatial distribution of ore deposit.

4. Multi-Fractal Characteristics of Fault Structure Spatial Distribution

4.1. Calculation Method

Multi-fractal is the mutual entanglement and mosaic of multiple single fractals in space. It is a generalization of single fractals [92,93] that can reflect more complex spatial structures [94]. The calculation of a multi-fractal function spectrum is the core of multi-fractal research, and is usually expressed as the functional relationship between the holder singularity exponent and

fractal dimension. It is generally described by the curve between α–$f(\alpha)$. Methods of calculating the multi-fractal function spectrum include the quadratic moment method, moment method, multiplier method, histogram method, and wavelet method, among others [63,95–99]. The most mature and widely used method is the moment method.

The steps for calculating the multi-fractal spectral function $f(\alpha)$ by the moment method are as follows:

(1) Define the fractal measure $P_i(r)$:

$$P_i(r) = \frac{n_i}{\sum\limits_{i=1}^{N(r)} n_i} \tag{7}$$

where r is the side length of the square grid covering the study area, i is the serial number of the grid at the r scale, n_i is the number of faults in the i-th grid, and $N(r)$ is the number of grids at the r scale.

(2) Build the multi-fractal partition function $X_q(r)$:

$$X_q(r) = \sum_{i=1}^{N(r)} P_i^q(r) \tag{8}$$

where q is an arbitrary number defined as the q-order moment of the fractal measure $P_i(r)$.

(3) Calculate the quality index $\tau(q)$:

$$\tau(q) = \lim_{r \to 0} \frac{\ln X_q(r)}{\ln r} = \lim_{r \to 0} \frac{\ln \sum\limits_{i=1}^{N(r)} P_i^q(r)}{\ln r} \tag{9}$$

In actual calculation, for an arbitrarily determined q value, the quality index $\tau(q)$ is obtained by calculating the slope of the best straight line fitted by the projected points ($\ln r$, $\ln X_q(r)$) at different scales r.

(4) Calculate the singularity index $\alpha(q)$:

$$\alpha(q) = \frac{d\tau(q)}{dq} = \lim_{r \to 0} \frac{\sum\limits_{i=1}^{N(r)} P_i^q(r) \ln P_i(r)}{\ln r \sum\limits_{i=1}^{N(r)} P_i^q(r)} \tag{10}$$

In the actual calculation, for an arbitrarily determined q value, the singularity index $\alpha(q)$ is obtained by calculating the slope of the best straight line fitted by the projected points ($\ln r \frac{\sum\limits_{i=1}^{N(r)} P_i^q(r) \ln P_i(r)}{\sum\limits_{i=1}^{N(r)} P_i^q(r)}$) at different scales r.

(5) Calculate the multi-fractal spectral function $f(\alpha)$:

$$f(\alpha) = q\alpha(q) - \tau(q) = q\frac{d\tau(q)}{dq} - \tau(q) \tag{11}$$

The singularity index $\alpha(q)$ and the multi-fractal spectral function $f(\alpha)$ reflect the local characteristics of the multi-fractal. The singularity index $\alpha(q)$ represents the fractal dimension of the small area of the fractal body, and its increment $\Delta\alpha$ (multi-fractal spectral width) describes the degree of inhomogeneity of the distribution of the subsets formed by the relevant physical quantities on the multi-fractal set. That is to say, it reflects the unevenness of the probability measure distribution on the entire fractal structure, and is used to describe the fluctuation range of the data set. The multi-fractal spectral function $f(\alpha)$ is a spectrum composed of infinite sequences composed of different singularity exponents $\alpha(q)$, which

can describe the changing trend of the number of elements in the subset formed by the multi-fractal and related physical quantities. Its increment $\Delta f(\alpha)$ (multi-fractal spectrum height) describes the magnitude of variation in the number of elements in the subset formed by the relevant physical quantity.

4.2. Multi-Fractal Characteristics of Fault Structures

When carrying out the multi-fractal spectrum calculation for the fault structures in the study area, the fractal scale interval used was 3.670–58.716 km, the q-order moment was −10 to 10, and the step size was 0.5. The calculation results are shown in Table 8. According to the fault multi-fractal spectrum data in the study area (Table 8), we drew the multi-fractal spectrum in the study area (Figure 6).

Table 8. Fault multifractal spectrum data table for the study area.

Serial Number	q	$\alpha(q)$	$f(\alpha)$	Serial Number	q	$\alpha(q)$	$f(\alpha)$
1	−10.0	1.0141	2.4020	22	0.5	1.5130	1.5203
2	−9.5	1.0150	2.3935	23	1.0	1.5390	1.5390
3	−9.0	1.0161	2.3831	24	1.5	1.5463	1.5475
4	−8.5	1.0175	2.3713	25	2.0	1.5383	1.5328
5	−8.0	1.0191	2.3572	26	2.5	1.5184	1.4876
6	−7.5	1.0212	2.3410	27	3.0	1.4900	1.4092
7	−7.0	1.0237	2.3233	28	3.5	1.4564	1.2999
8	−6.5	1.0267	2.3031	29	4.0	1.4211	1.1675
9	−6.0	1.0306	2.2787	30	4.5	1.3867	1.0214
10	−5.5	1.0355	2.2506	31	5.0	1.3553	0.8724
11	−5.0	1.0418	2.2176	32	5.5	1.3279	0.7288
12	−4.5	1.0503	2.1773	33	6.0	1.3048	0.5961
13	−4.0	1.0618	2.1286	34	6.5	1.2858	0.4775
14	−3.5	1.0782	2.0673	35	7.0	1.2703	0.3730
15	−3.0	1.1018	1.9910	36	7.5	1.2580	0.2840
16	−2.5	1.1360	1.8974	37	8.0	1.2481	0.2073
17	−2.0	1.1843	1.7894	38	8.5	1.2404	0.1434
18	−1.5	1.2480	1.6786	39	9.0	1.2343	0.0907
19	−1.0	1.3235	1.5845	40	9.5	1.2296	0.0472
20	−0.5	1.4003	1.5268	41	10.0	1.2260	0.0120
21	0.0	1.4662	1.5095				

The graph connecting points $(q, \alpha(q), f(\alpha))$ in the three-dimensional coordinate system is a spiral curve (Figure 6a), and the nonlinear relationship is obvious. When the q-order moment is −10 to 10, the singularity index $\alpha(q)$ ranges from 1.0141 to 1.5463; it first increases and then decreases with the increase of the order moment q (Figure 6e). At the same time, $f(\alpha)$ ranges from 0.0120 to 2.4020, and decreases as a whole and increases locally with the increase of the order moment q (Figure 6d). The curve connected by points $(\alpha(q), f(\alpha))$ is not a common parabolic (or hook) shape with downward opening, but a combination of two semi-parabolic shapes with opposite opening directions (i.e., a bifurcation; Figure 6b). When the q-order moment ranges from 1 to 10, the curve connecting the points $(\alpha(q), f(\alpha))$ is a typical semi-parabolic shape (Figure 6c).

When the q-order moment is between −10 and 10, the shape of the multi-fractal spectrum is quite different from that reported in most previous literatures. Most multi-fractal spectrum parameter calculations in the literature adopted the fitting method, such as the singularity index $\alpha(q)$, etc., and did not strictly use the limit method for calculation (which cannot be realized); this increases the multi-fractal spectrum shape diversity to a certain extent. Various shapes of multi-fractal spectra have been reported. In addition to the typical downward-opening parabola or hook, there can also be zigzag [100] and bifurcated [101–103]. The main reasons for the diverse shapes of multi-fractal spectra are as follows: (1) the characteristics and differences of the calculation method itself; (2) differences

in tectonic distribution characteristics (or element enrichment methods) in different regions; (3) differences in the value range of the q-order moment; and (4) buried fault structures were not discovered. When using the same calculation method to calculate the multi-fractal spectrum, in addition to the characteristics of the fractal itself, the value of the q-order moment is also an important factor.
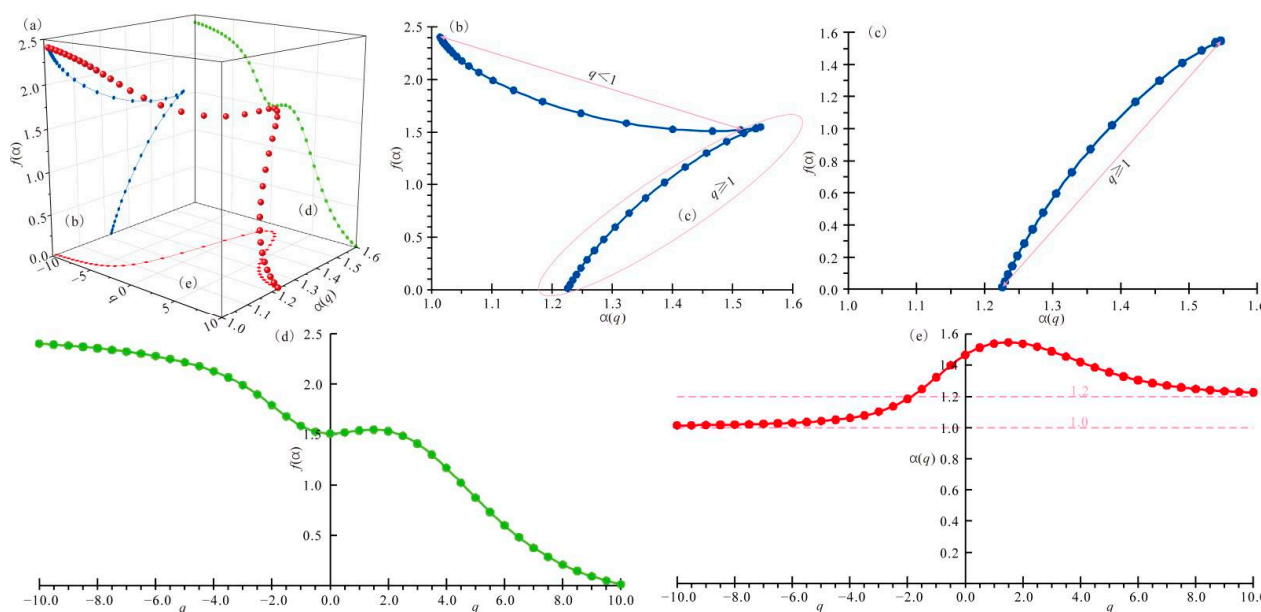

Figure 6. Multi-fractal spectrum of faults in the study area. (**a**) 3-D plot of q, $\alpha(q)$, $f(\alpha)$, showing points $(q, \alpha(q), f(\alpha))$ in the three-dimensional coordinate system is a spiral; (**b**) 2-D plot of $\alpha(q)$, $f(\alpha)$, showing the curve connected by points $(\alpha(q), f(\alpha))$ is not a common parabolic (or hook) shape with downward opening, but a combination of two semi-parabolic shapes with opposite opening directions; (**c**) When the q-order moment ranges from 1 to 10, the curve connecting the points $(\alpha(q), f(\alpha))$ is a typical semi-parabolic shape; (**d**) $f(\alpha)$ ranges from 0.0120 to 2.4020, and decreases as a whole and increases locally with the increase of the order moment q; and (**e**) the singularity index $\alpha(q)$ first increases and then decreases with the increase of the order moment q.

Theoretically, the value of the q-order moment can be any real number, but there is no uniform standard when carrying out multi-fractal spectrum calculations, and the numerical ranges used in different studies vary greatly. The multi-fractal spectrum uses different q-order moment values to describe the characteristics of different levels of the fractal body. When q is greater than 0, the multi-fractal spectrum can describe the basic characteristics of the fractal body. When q is less than 0, the multi-fractal spectrum focuses on the properties of low-probability regions, reflecting small structural changes in the fractal structure. The smaller q is, the more easily affected it is by measurement errors or interference factors. As most previous studies carried out parameter calculation on parabolic or hooked fractal spectrum, in order to ensure the reliability of this calculation, we only calculated $\Delta f(\alpha)$ and $\Delta \alpha$ of the multi-fractal spectrum when the q-order moment was between 1 and 10. Where $\Delta \alpha = \alpha_{\max} - \alpha_{\min}$, $\Delta f(\alpha) = f(\alpha)_{\max} - f(\alpha)_{\min}$. When $\alpha_{\max} = 1.5463$, $\alpha_{\min} = 1.2260$, $f(\alpha)_{\max} = 1.5475$, and $f(\alpha)_{\min} = 0.0120$, then $\Delta \alpha = \alpha_{\max} - \alpha_{\min} = 0.3203$, $\Delta f(\alpha) = f(\alpha)_{\max} - f(\alpha)_{\min} = 1.5355$, implying that the study area has great metallogenic potential.

5. Fractal Clustering Characteristics of Ore Deposits

5.1. Fractal Characteristics of Spatial Distribution of Ore Deposits

The 48 subdivisions of the EGMB contain 61 metal deposits, including 53 Pb–Zn deposits. Metal deposits are distributed in 27 subdivisions, including 1-2, 2-4, 3-3, 3-4, 6-1, 6-2, 6-3, and 6-4, etc., accounting for 56.3% of the total subdivisions. Among them, there are 30 metal ore deposits in seven subdivisions including 1-2, 5-4, 7-2, 8-1, 8-4, 12-2, and 11-3,

accounting for ~49.2% of the total number of metal deposits. Pb–Zn deposits are distributed in 24 subdivisions, including 1-2, 2-4, 3-3, 3-4, 6-1, 6-2, 6-3, and 6-4, accounting for 50% of the total number of subdivisions. Among them, seven subdivisions including 1-2, 5-4, 7-2, 8-1, 8-4, 12-2, and 11-3 have developed 27 Pb–Zn deposits, accounting for 50.9% of all Pb–Zn deposits. In summary, deposits are mainly distributed in a small number of subdivisions, and from a qualitative perspective, deposit distribution has significant clustering.

Taking ore deposits as a point set, the spatial distribution fractal dimension (SDD) of ore deposits can be calculated by the counting-box method, similar to that applied to the treatment of CPD values for fault systems described in the previous sections. The statistics of the calculation parameters of the SDD values are shown in Table 9. According to Table 9, Figure 7 shows the ln$r$–ln$N(r)$ regression fitting line graph. From the statistical table of the SDD value of mineral deposits in some areas of China (Table 10) and the linear fitting diagram of the SDD value calculation of mineral deposits (Figure 7), it can be seen that: (1) the fitting degrees of the linear fitting lines of Sb deposits, Pb–Zn deposits, and metal deposits in the study area are all greater than 0.97, indicating that their spatial distributions have fractal cluster structures; (2) the SDD value of metal deposits is greater than that of Pb–Zn deposits, while the SDD value of Pb–Zn deposits is greater than that of Sb deposits; (3) the metal deposits and Pb–Zn deposits in the study area have a smaller SDD than most other regions in China with larger fractal scales (upper limit). Compared with the same fractal scale (upper limit) of Pb–Zn deposits in the Yadu–Mangdong metallogenic belt, the SDD is also smaller, indicating that the metal deposits and Pb–Zn deposits in the study area are more clustered; and (4) the clustering of the ore deposits results in decreasing SDD, while the SDD of the ore deposits is much smaller than those of the integrated faults and NE-trending faults in the study area.

Table 9. Statistical table of calculation parameters for the spatial distribution fractal dimensions (SDD) of deposits.

Deposit Category	Fractal Scale, *r* (km)	*N(r)*	ln*r*	ln*N(r)*
Metal deposits	58.716	10	4.073	2.303
	29.358	30	3.380	3.401
	14.679	55	2.686	4.007
	7.340	97	1.993	4.575
Pb–Zn deposits	58.716	10	4.073	2.303
	29.358	27	3.380	3.296
	14.679	48	2.686	3.871
	7.340	87	1.993	4.466
Sb deposits	58.716	3	4.073	1.099
	29.358	5	3.380	1.609
	14.679	7	2.686	1.946
	7.340	9	1.993	2.197

5.2. Fractal Characteristics of Deposit Quantity and Density

An important step in the exploration of ore deposits is to investigate the distribution characteristics of known ore deposits within an area delineated by a finite distance [58,104].

To quantitatively determine the distribution character of ore deposits within a circular area of radius *r*, we normally adopted a probability density function defined as:

$$d(r) = Kr^{D_D-2} \quad (2 > D_D > 0) \tag{12}$$

where $d(r)$ is the probability density function, denoting the number of ore deposits per unit area within radius *r*, taking a known ore deposit as the center of the circle; K is a constant; and D_D is the density distribution fractal dimension (DDD). In a non-scale section, the higher the D_D value, the greater the number of ore deposits [58,106].
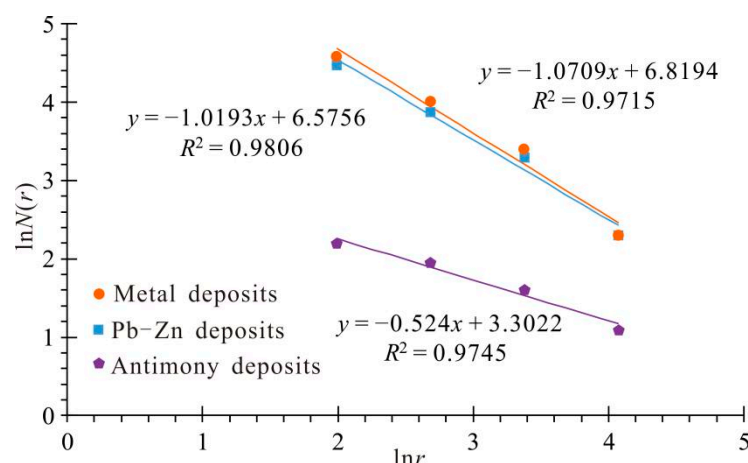
Figure 7. Linear fitting graph for spatial distribution fractal dimensions (SDD) calculation of ore deposits.

Table 10. Statistical table of spatial distribution fractal dimensions (SDD) values of deposits in some areas of China.

Location	Kinds of Minerals	Scale Interval (km)	SDD	References
Anhui Province	Coal, Copper, Iron, etc	17. 8125–285	1.3371	[59]
South China	Uranium	20–400	1.0468	[80]
Western and Northern Yunkai Uplift	Gold	1.25–10	0.3552	[58]
		10–160	1.2418	
China	Gold	20–150	0.2293	[104]
		150–5000	1.3073	
Zhejiang Province	Gold	1–20	0.1923	[105]
		20–750	0.7168	
	Fluorite	1–20	0.3778	
		20–750	1.1851	
	Pb and Zn	1–20	0.1459	
		20–750	1.1723	
Altai Region of Xinjiang	Gold, Copper, Pb, Zn, etc.	1.25–16.32	0.2305	[56]
		16.32–150	1.512	
Yadu–Mangdong metallogenic belt	Pb and Zn	6.741–53.930	1.3262	this article
EGMB	Pb and Zn	7.34–58.716	1.0193	this article
	Sb	7.34–58.716	0.5240	this article
	Pb, Zn, Sb, etc.	7.34–58.716	1.0709	this article

The quantity fractal distribution function is proposed to represent quantitatively the number of possible ore deposits $N(r)$ that is likely to be explored within a definite radius from the center:

$$N(r) = Lr^{D_S} \tag{13}$$

where $N(r)$ is the quantity distribution function, denoting the number of ore deposits within radius r, taking a known ore deposit as the center of the circle; L is a constant; and D_S is the quantity distribution fractal dimension (QDD).

In practical calculation, we took 10 ore deposits with a relatively uniform distribution as the center of the circle. The number and density of the ore deposits covered by areas of various radius, r, were calculated and we took the averaged values of 10 deposit centers (Table 11). Finally, the data were fitted (Figure 8).

Within a research scale of 20 to 80 km, Pb–Zn and all metals deposits versus the average number of deposits show power-law relationships, and the coefficients of determination are 0.9906 and 0.9966, respectively, indicating a high degree of fit. The number distributions of Pb–Zn and all metals deposits have fractal structures, and the QDD values are 1.4225 and 1.4716, respectively (Figure 8a). The Pb–Zn and all metals deposits versus the deposit density also have power-law relationships, and the determination coefficients are 0.9454

and 0.9742, respectively, indicating a high degree of fit. The density distributions of the Pb–Zn and all metals deposits have fractal structures, and the DDD values are 1.422 and 1.472, respectively (Figure 8b). For the fractal distribution of both number of deposits and density of deposits, the fractal dimension values of Pb–Zn and all metals deposits are high (>1.42), indicating high clustering.

Table 11. Statistics of fractal distribution data of deposit number and density.

Fractal Scale, *r* (km)	Pb–Zn Deposits		Metal Deposits	
	Average Number	Density (No./km²)	Average Number	Density (No./km²)
20	3.1	0.00248	3.3	0.00264
30	4.5	0.00160	5.4	0.00192
40	7.1	0.00142	8.5	0.00170
50	10.3	0.00132	12	0.00153
60	14.2	0.00126	16.9	0.00150
70	17	0.00111	20.1	0.00131
80	20.4	0.00102	23.8	0.00119
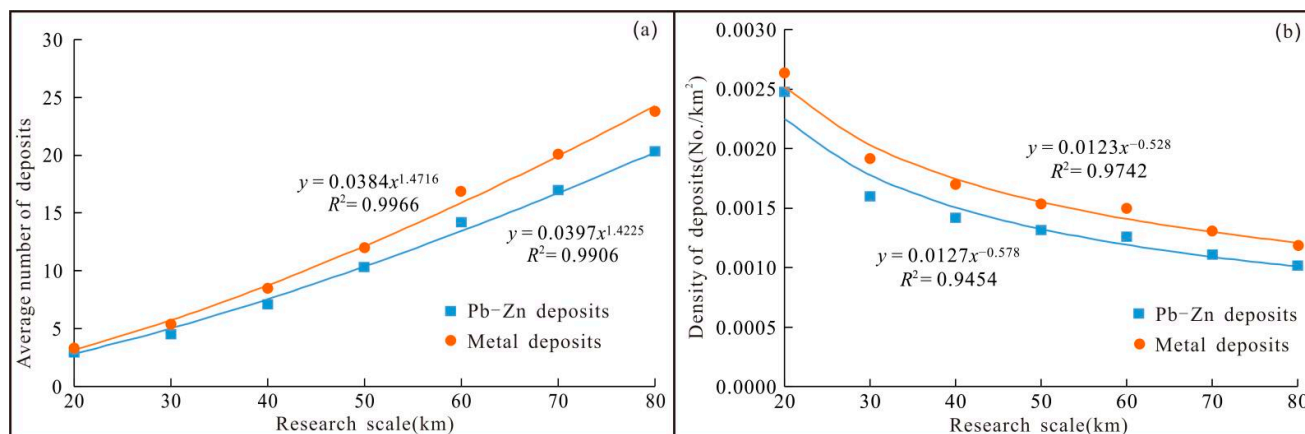
Figure 8. Fitting diagram of fractal distribution for deposit number (**a**) and density (**b**).

6. Coupling Law of Fault Fractal Characteristics and Spatial Distribution of Ore Deposits

According to the theory of self-organized criticality, a fracture system with fractal characteristics is formed by the connection, evolution, and spontaneous organization of small fractures to a point during the dissipation process of the fracture, so that the strain is concentrated on the main fault zone with fractal geometry. The fault fractal dimension value is related to its connectivity. When the fractal dimension value of the fault is lower than the critical value, the deformation and permeability are low, the fault is isolated, and the fault connectivity is poor. When the fractal dimension of the fault reaches or exceeds the critical value, deformation is strong, permeability increases, and the connectivity of the fault is good, which is conducive to the migration and accumulation of ore-forming fluids and the formation of hydrothermal deposits. Numerical simulations of biaxial compression tests of rock blocks show that the critical value of the fractal dimension is 1.22 to 1.38 [77]. The fault fractal dimension value has some locality (relative to the study scale). However, since the scale of the study roughly matches the scale of the study area, and the scale of the study area basically matches the scale of the structure, the critical value of the fractal dimension of the fault still has certain reference significance for this study; that is, areas with the fault CPD values of >1.22 are conducive to mineralization.

The distribution of hydrothermal deposits is not only controlled by fault factors, but also by favorable lithology (or lithologic combination) and others. In this study, the fault CPD of the subdivisions with developed ore deposits is mostly greater than 1.22, but for

some subdivisions with ore deposits it is less than and very close to 1.22. This confirms that the distribution of metal deposits is mainly controlled by faults, and confirms the reliability of distribution analysis using fractal dimension value. From a qualitative perspective, the neighborhood fractal dimension values of the subdivisions of various metal deposits are generally relatively low, which may be because neighborhood areas with relatively low fractal dimension values are conducive to blocking and sealing ore-forming fluids. In fact, owing to the clustered distribution of ore deposits, ore deposits are often developed in two or more consecutive subdivisions. Such subdivisions should to be regarded as a whole so as to understand the role of adjacent regions in blocking and sealing ore-forming fluids. Taking the CPD values as an example, we drew a horizontal and vertical fluctuation diagram of subdivision CPD values (Figure 9). The subdivision or subdivision complex of developed deposits are adjacent to at least one subdivision with a relatively low fractal dimension value in a two-dimensional perspective.
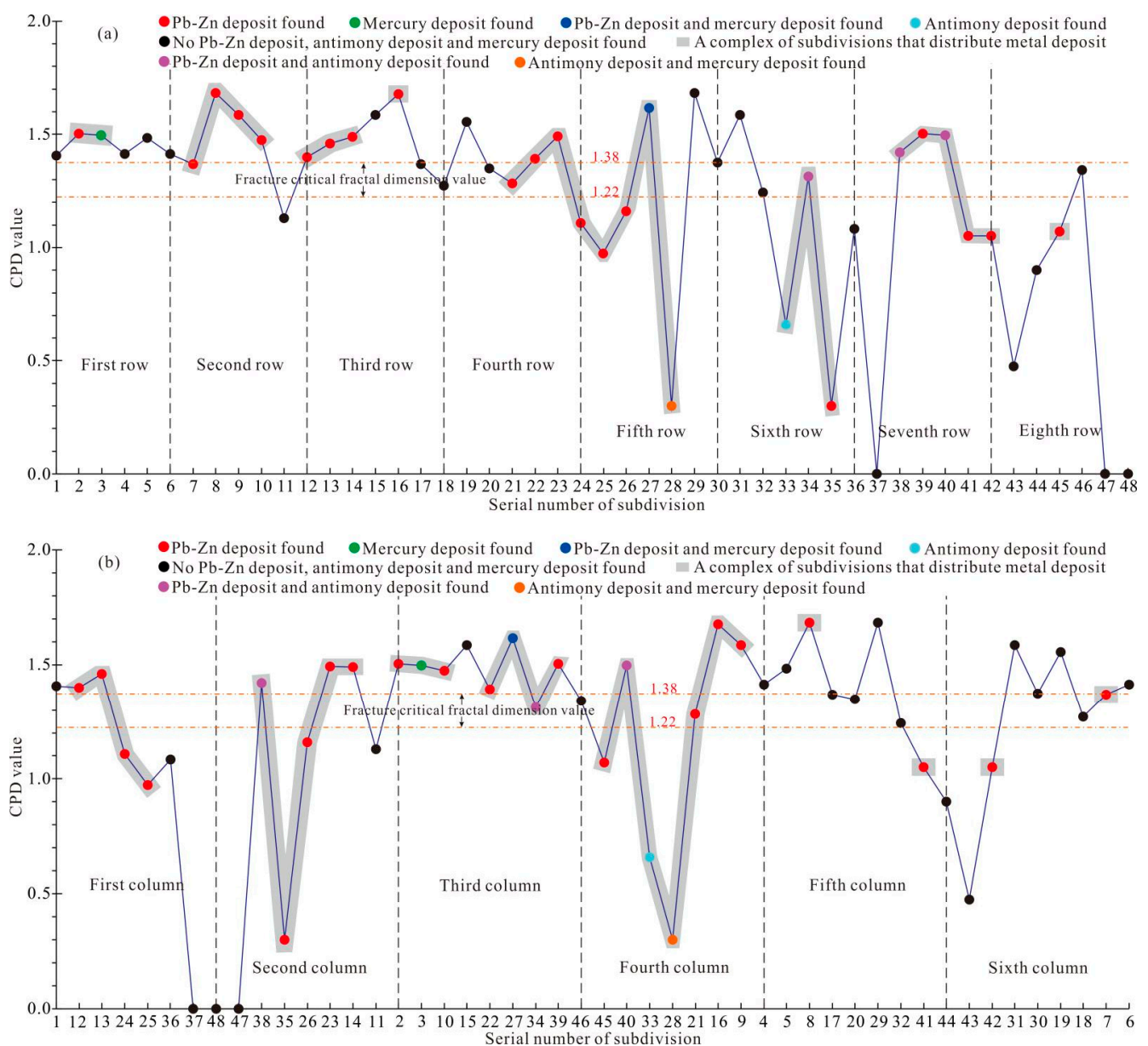
Figure 9. Vertical and horizontal wave graphs of fractal dimensions. (**a**) Horizontal wave graphs of fractal dimensions; and (**b**) Vertical wave graphs of fractal dimensions.

To systematically explore the relationship between the distribution of deposits and the fractal dimension value, a projection map of the fractal dimension value of the subdivision and number of deposits was drawn (Figure 10), along with a projection map of different types of fractal dimension values of the subdivision (Figure 11). The favorable fractal dimension distribution intervals of Pb–Zn and all metals deposits are basically the same; both are mainly distributed in ore-bearing subdivisions that simultaneously satisfy three conditions: CPD > 1.16, IND > 0.95, and CRD > 0.97.
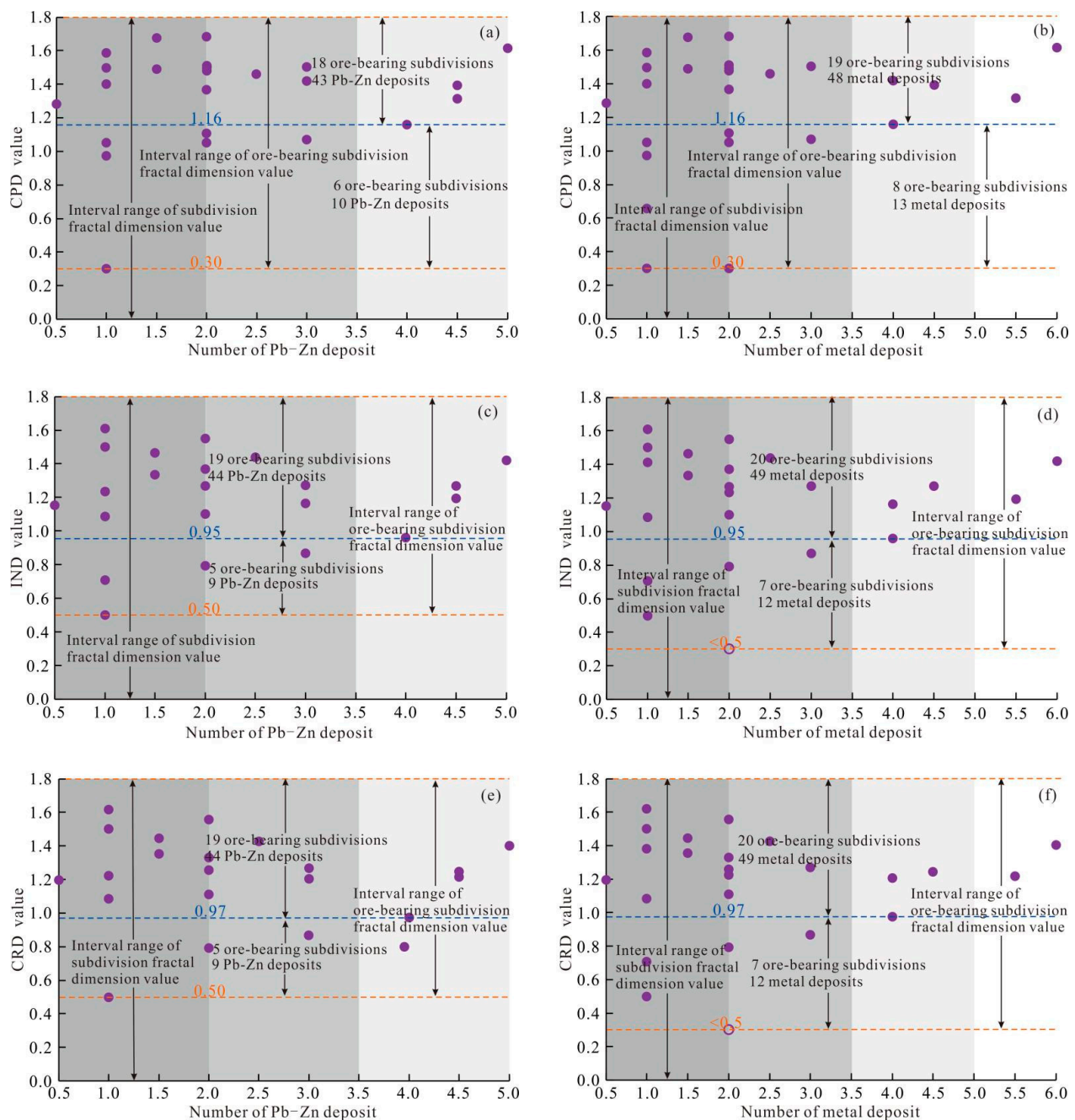
Figure 10. Subdivision projection maps of deposit quantity versus fractal dimension. (**a**) Subdivision projection maps of Pb–Zn deposit quantity versus CPD; (**b**) Subdivision projection maps of all metals deposits quantity versus CPD; (**c**) Subdivision projection maps of Pb–Zn deposit quantity versus IND; (**d**) Subdivision projection maps of all metals deposits quantity versus IND; (**e**) Subdivision projection maps of Pb–Zn deposit quantity versus CRD; and (**f**) Subdivision projection maps of all metals deposits quantity versus CRD.
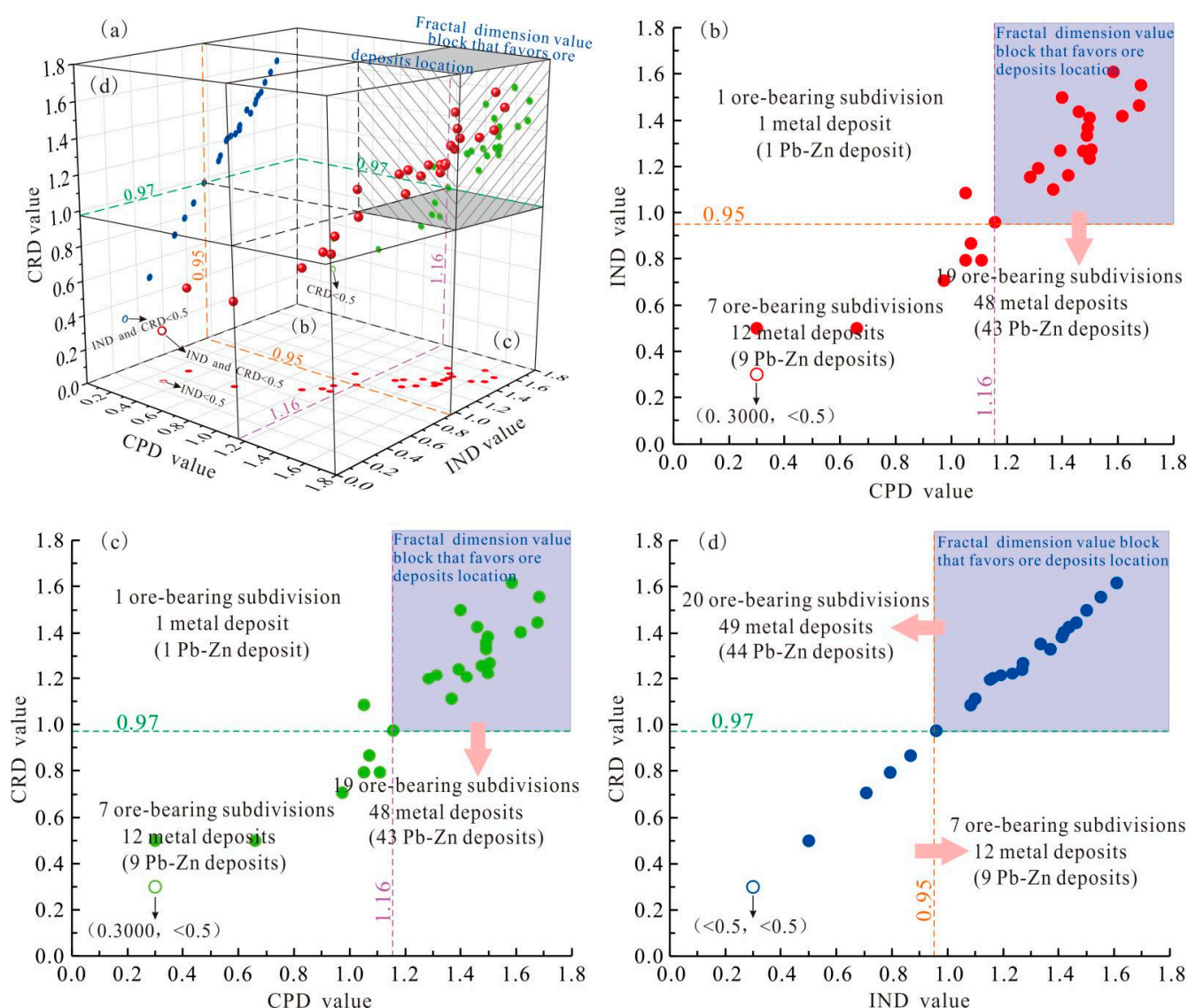
Figure 11. Different types of fractal dimension projection maps of subdivisions. (**a**) 3-D plot of CPD, IND, CRD of ore-bearing subdivision; (**b**) CPD versus IND plot of ore-bearing subdivision; (**c**) CPD versus CRD plot of ore-bearing subdivision; and (**d**) IND versus CRD plot of ore-bearing subdivision.

7. Prediction of Favorable Areas for Prospecting

7.1. Fractal Dimension Value Analysis

From the perspective of fractal dimension value, areas favorable for the distribution of ore deposits should satisfy two conditions: (1) CPD > 1.16, IND > 0.95, and CRD > 0.97; and (2) on a two-dimensional plane, there are adjacent regions that relatively block fluid flow. Favorable prospecting areas based on CPD, IND, and CRD were delineated (Figure 12a–c), and their overlapping area was taken as the comprehensive favorable metallogenic area (Figure 12d).

7.2. Fry Analysis

Fry analysis was first developed for mineral rock stress analysis [107–110], and was subsequently extended to measure the spatial distribution of ore deposits and infer potential ore-controlling structures [111–113]. The basic principles of the Fry analysis method are as follows. Assuming that there are n points in a known plane A, copying the plane n times can obtain n identical planes $A_1, A_2, \ldots A_n$. Select a point in plane A_1 as a reference point to establish a rectangular coordinate system, and arbitrarily select a point other than the

reference point in plane A_2, and place it at the coordinate origin of plane A_1. Similarly, a point is arbitrarily selected from the remaining n-2 points in plane A_3 and placed at the coordinate origin of plane A_1. The above process is repeated until each point coincides with the coordinate origin of plane A_1, and finally n(n-1) points are generated in the plane. Fry analysis is a spatial autocorrelation method used to study the distribution trend of spatial points. In practical application, the areas with more deposit distribution tend to have dense Fry points, so favorable metallogenic areas can be divided according to the relative number of Fry points' distribution at the macro scale. In this study, we applied Fry analysis to the 61 known metal deposits, including 53 Pb–Zn deposits, 5 Sb deposits, and 3 Hg deposits. The Fry projection was obtained by 61 shots (Figure 13a,b). According to the number of projected ore deposit points in the subdivision, the favorable metallogenic areas of Pb–Zn ores and Sb–Hg ores were identified (Figure 13c,d). From Figure 14, the metallogenic potential of Pb–Zn deposits decreases in the following order: subdivisions 5-4 and 8-1 > 9 subdivisions, including 6-3, 6-2; and 5-1 > 8 subdivisions, including 1-2, 1-3, and 7-2. For Sb–Hg deposits, nine subdivisions, including 5-2, 5-3, and 8-2, have relatively great metallogenic potential. Most favorable metallogenic subdivisions of Sb–Hg deposits are also favorable metallogenic areas of Pb–Zn deposits, indicating strong spatial consistency.

7.3. Prediction of Comprehensive Favorable Metallogenic Areas

Dispersed metals in the study area are mainly enriched in Pb–Zn deposits or Pb–Zn poly-metallic deposits, and so favorable metallogenic areas of Pb–Zn are also favorable metallogenic area of dispersed metals. According to importance, the comprehensive favorable metallogenic areas of Pb–Zn were divided into four grades (Figure 14a), while those of Sb–Hg were divided into two grades (Figure 14b). Grade I denote common overlap of fractal dimension value comprehensive favorable metallogenic areas and subdivisions with > 70 Pb–Zn deposits after Fry's projection. Most known deposits are distributed in this area, which has the greatest prospecting potential. Grade II areas are those comprehensive favorable metallogenic area with >100 Pb–Zn deposits after Fry's projection; these include seven known ore deposits. Grade III deposits are those subdivisions with 70–99 Pb–Zn deposits after Fry's projection. In space, these are mainly adjacent to grade I and grade II areas. The remaining subdivisions (50–69 Pb–Zn deposits after Fry's projection) are grade IV and have low prospecting potential.

The common overlap of the fractal dimension value analysis comprehensive favorable metallogenic area and subdivisions of the favorable distribution of Sb (or Hg) deposits after Fry's projection form the grade I favorable metallogenic areas of Sb (or Hg). This includes three areas with the greatest prospecting potential. The remaining comprehensive favorable metallogenic areas and subdivisions of the favorable distribution of Sb (or Hg) deposits after Fry's projection are grade II.
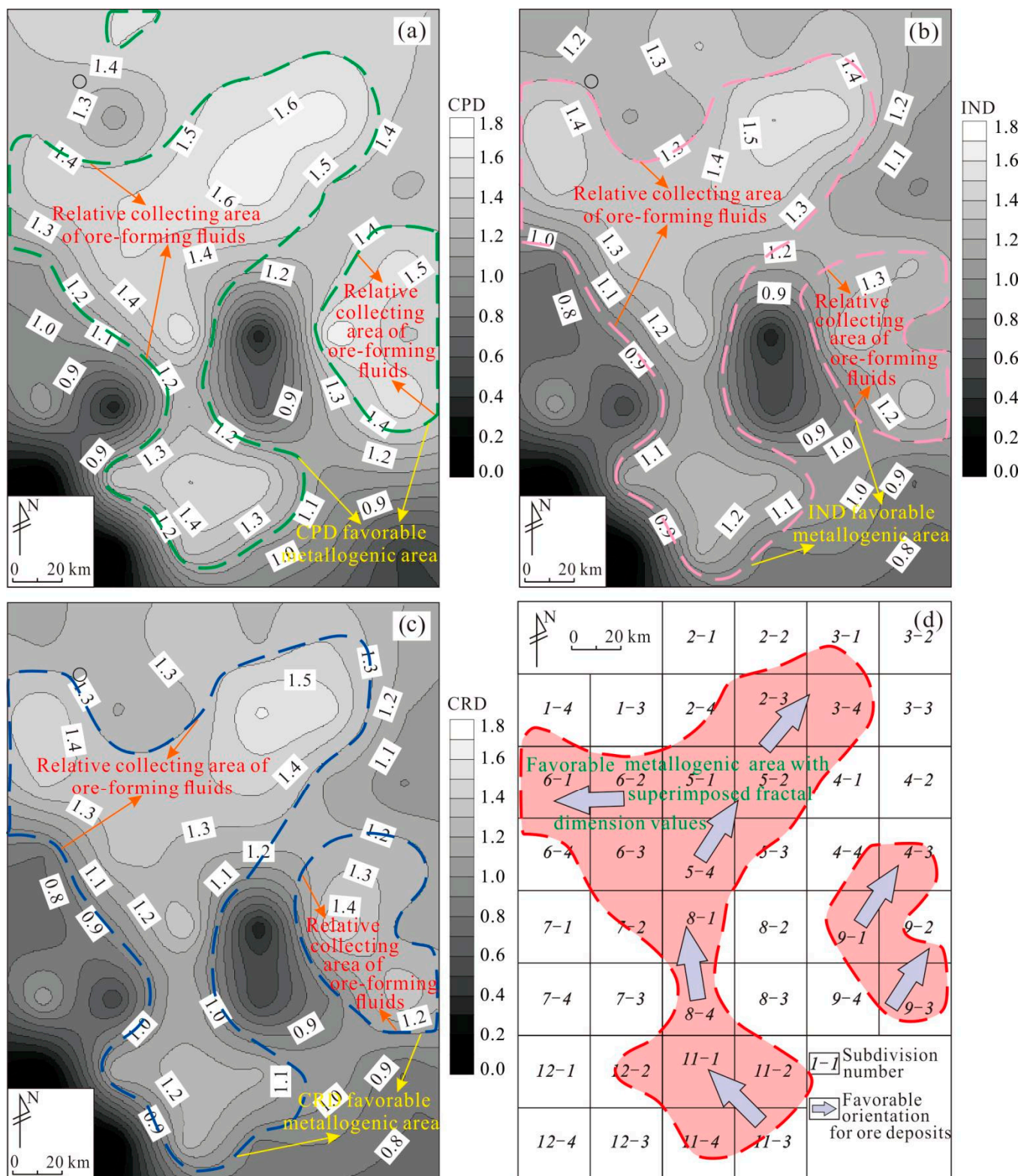
Figure 12. Fractal dimension favorable mining area. (**a**) CPD of fault favorable mining area; (**b**) IND of fault favorable mining area; (**c**) CRD of fault favorable mining area; and (**d**) Comprehensive consideration of fault fractal dimension value for favorable metallogenic area.
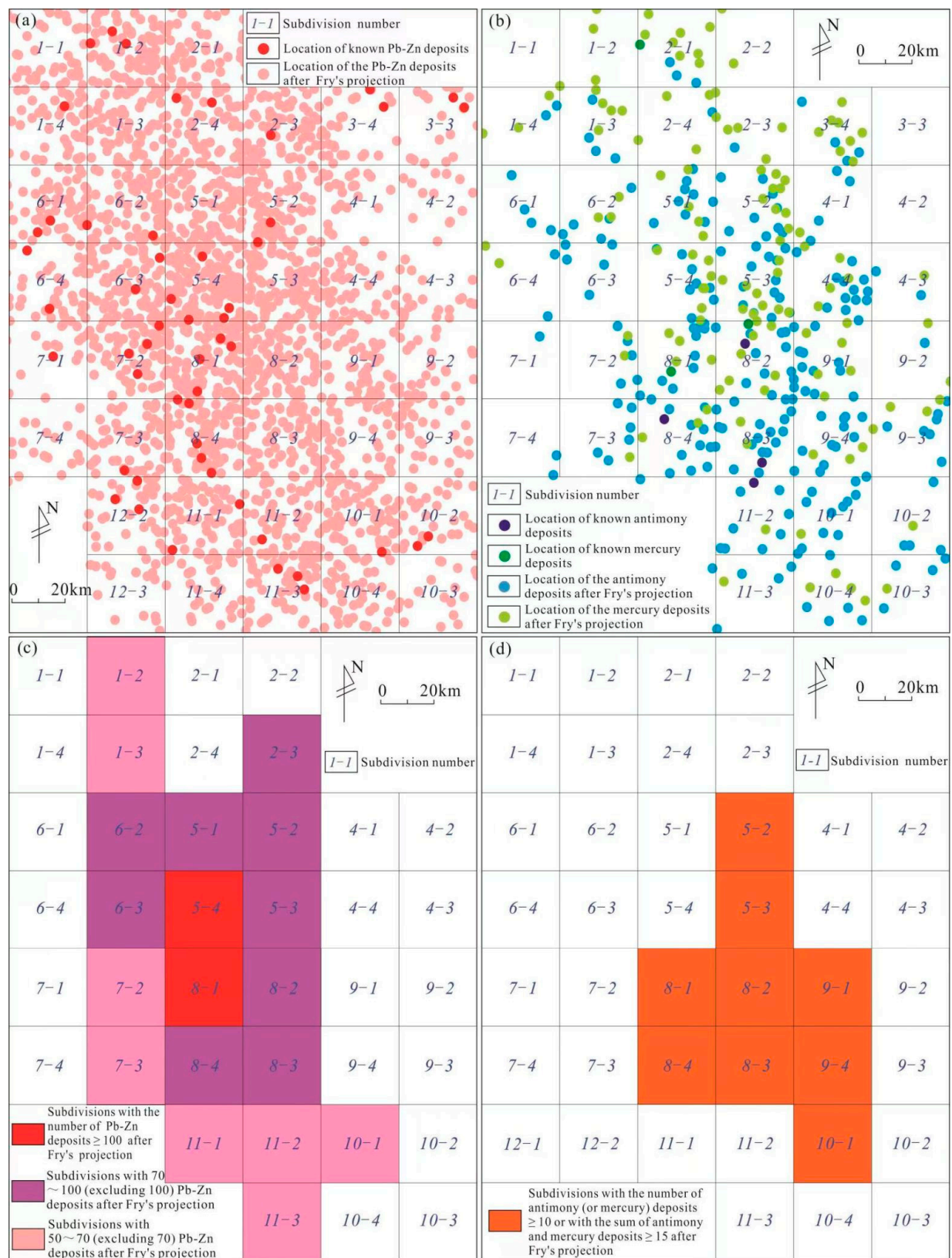
Figure 13. Fry analysis map of the deposit. (**a**) Fry analysis diagram of Pb–Zn deposits; (**b**) Fry analysis diagram of Sb–Hg deposits; (**c**) Fry point distribution map of Pb–Zn deposits; and (**d**) Fry point distribution map of Sb–Hg deposits.
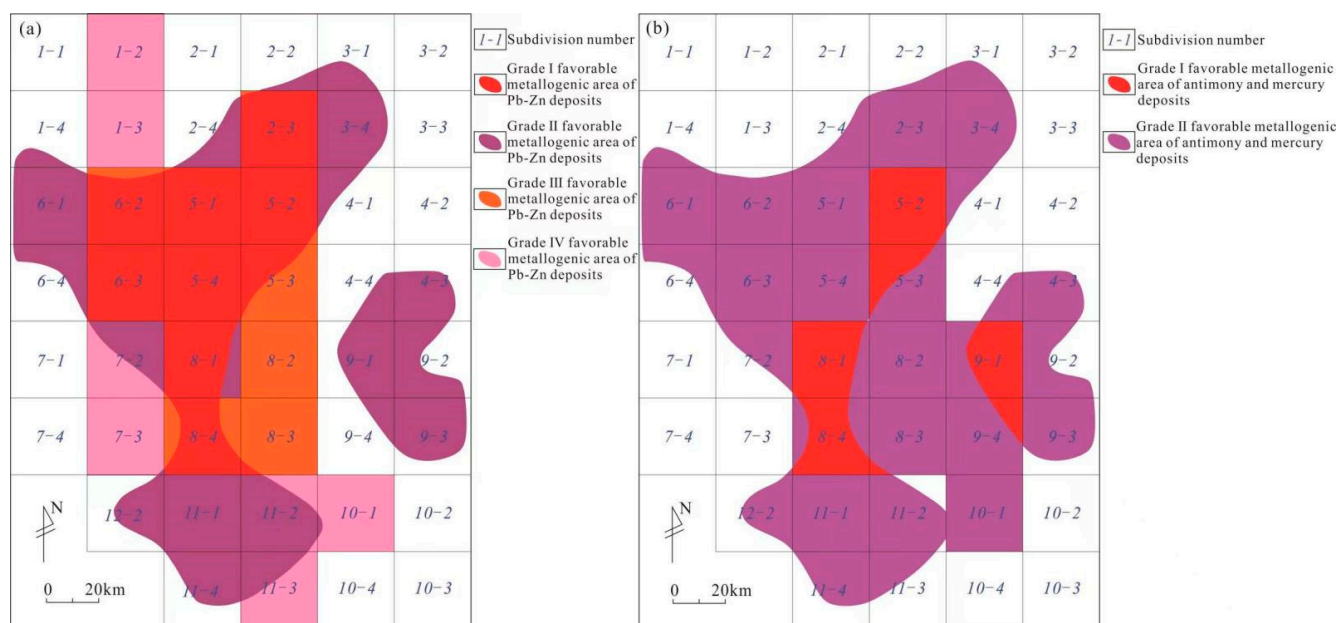
Figure 14. Distribution map of comprehensive favorable metallogenic areas. (**a**) Distribution map of Pb–Zn deposits comprehensive favorable metallogenic areas and (**b**) Distribution map of Sb–Hg deposits comprehensive favorable metallogenic areas.

8. Conclusions

(1) In the scale range of 3.670–58.716 km, fault structures in the EGMB have good statistical self-similarity. The integrated faults CPD is 1.5095, the IND is 1.5391, and the CRD is 1.5436, indicating fault structures with high maturity, which are conducive to the migration and accumulation of ore-forming fluids.

(2) When the *q*-order moment ranges from 1 to 10, $\Delta\alpha$ is 0.3203 and $\Delta f(\alpha)$ is 1.5355, implying that the study area has great metallogenic potential.

(3) Within the scale range of 7.340–58.716 km, the SDD values of Sb, Pb–Zn, and other metal deposits are 0.5240, 1.0193, and 1.0709, respectively. Within the scale of 20–80 km, the number and density distributions of Pb–Zn and metal deposits are all fractal structures; the QDD values are 1.4225 and 1.4716, respectively, and the DDD values are 1.422 and 1.472, respectively, indicating high clustering of both Pb–Zn and other metal deposits.

(4) From the perspective of fractal dimension value, areas favorable for the distribution of ore deposits should satisfy two conditions: (1) CPD > 1.16, IND > 0.95, and CRD > 0.97; and (2) on the two-dimensional plane, the fractal dimension value of the adjacent area is lower (i.e., adjacent regions relatively block fluid flow).

(5) The comprehensive favorable metallogenic areas of Pb–Zn and associated dispersed metals are divided into four grades. Among them, favorable metallogenic region of grade I is continuously distributed in space. Most known deposits are distributed in this area, and the prospecting potential is the greatest.

Data Availability Statement: The data presented in this study are available on reasonable request from the corresponding authors.

Conflicts of Interest: The authors declare no conflict of interest.

References

1.　Zhang, C.Q.; Rui, Z.Y.; Chen, Y.C.; Wang, D.H.; Chen, Z.H.; Lou, D.B. The main successive strategic bases of resources for Pb–Zn deposits in China. *Geol. China* **2013**, *40*, 248–272. (In Chinese)
2.　Ye, L.; Hu, Y.S.; Yang, S.P.; Wei, C.; Yang, X.Y.; Li, Z.L.; An, Q.; Lu, M.D. A discussion on the Pb–Zn mineralization of the Qiandong metallogenic belt. *Acta Mineral. Sin.* **2018**, *38*, 709–715. (In Chinese)
3.　Li, K.; Liu, F.; Zhao, W.Q.; Zhao, S.R.; Tang, Z.Y.; Duan, Q.F.; Cao, L. Metallogenic Model of Carbonate-Hosted Pb–Zn Deposits in West Hunan and East Guizhou Provinces, South China. *Earth Sci.* **2021**, *46*, 1151–1172. (In Chinese)
4.　Liu, W.J.; Zheng, R.C. Characteristics and Movement of Ore-Forming Fluids in the Huayuan Lead-Zinc Deposit. *Miner. Depos.* **2000**, *19*, 173–181. (In Chinese)
5.　Yang, S.X.; Yu, P.R.; Lao, K.T. Metallogenic regularity and prospecting direction of lead-zinc deposits in northwestern Hunan. *Land Resour. Her.* **2006**, *3*, 92–98. (In Chinese)
6.　Hu, Y.S.; Ye, L.; Wei, C.; Li, Z.L.; Huang, Z.L.; Wang, H.Y. Trace elements in sphalerite from the Dadongla Zn-Pb deposit, western Hunan–eastern Guizhou Zn-Pb metallogenic belt, south China. *Acta Geol. Sin.* **2020**, *94*, 2152–2164. [CrossRef]
7.　Tang, Z.Y.; Deng, F.; Li, K.; Duan, Q.F.; Zou, X.W.; Dai, P.Y. Stratigraphic characteristics of the Cambrian Qingxudong formation in relation to lead-zinc mineralization in western Hunan-eastern Guizhou area. *Geol. China* **2012**, *39*, 1034–1041. (In Chinese)
8.　Mao, D.L. Geological Characteristics and Genesis of the Danaopo Pb–Zn Deposit in Huayuan County, Hunan Province. *Mod. Min.* **2016**, *32*, 90–94. (In Chinese)
9.　Schneider, J.; Boni, M.; Lapponi, F.; Bechstadt, T. Carbonate Hosted Zinc-Lead Deposits in the Lower Cambrian of Hunan, South China: A Radiogenic (Pb, Sr) Isotope Study. *Econ. Geol.* **2002**, *97*, 1815–1827. [CrossRef]
10.　Ye, L.; Pan, Z.P.; Li, C.Y.; Liu, T.G.; Xia, B. Isotopic Geochemical Characters in Niujiaotang Cd Rick Znic Deposit, Duyun, Guizhou. *Mineral. Petrol.* **2005**, *25*, 70–74. (In Chinese)
11.　Liu, J.S.; Zou, X.W.; Tang, C.Y.; Cui, S.; Xia, J.; Gan, J.M.; Zhao, W.Q.; Jin, S.C. Preliminary Discussion on Relationship between Pb–Zn Deposits and Paleo-oil Reservoirs in Western Hunan and Eastern Guizhou Province. *Geol. Miner. Resour. South China* **2012**, *28*, 220–225. (In Chinese)
12.　Cai, Y.X.; Yang, H.M.; Duan, R.C.; Lu, S.S.; Zhang, L.G.; Liu, C.P.; Qiu, X.F. Fluid Inclusions and S, Pb, C Isotope Geochemistry of Pb–Zn Deposits Hosted by Lower Cambrian in Western Hunan-Eastern Guizhou Area. *Geoscience* **2014**, *28*, 29–41. (In Chinese)
13.　Li, K.; Duan, Q.F.; Zhao, S.R.; Tang, Z.Y. Material sources and ore-forming mechanism of the Huayuan Pb–Zn ore deposit in Hu′nan Province: Evidence from S, Pb, Sr isotopes of sulfides. *Geol. Bull. China* **2017**, *36*, 811–822. (In Chinese)
14.　Yang, S.X.; Lao, K.T. A tentative discussion on genesis of lead-zinc deposits in northwest Hunan. *Miner. Depos.* **2007**, *26*, 330–340. (In Chinese)
15.　Zhou, Y.; Duan, Q.F.; Tang, J.X.; Cao, L.; Li, F.; Huang, H.L.; Gan, J.M. The Large-Scale Low-Temperature Mineralization of Lead-Zinc Deposits in Western Hunan-Evidence from Fluid Inclusions. *Geol. Explor.* **2014**, *50*, 515–532. (In Chinese)
16.　Yu, Y.S.; Guo, F.S.; Dai, Y.P.; Liu, A.S.; Zhou, Y. Ore genesis of Tangbian Pb–Zn deposit in Tongren, Guizhou: Evidence from ore-forming fluids and isotopes. *Miner. Depos.* **2017**, *36*, 330–344. (In Chinese)
17.　Li, K.; Zhao, S.R.; Tang, Z.Y.; Duan, Q.F.; Li, J.W. Fluid Sources and Ore Genesis of the Pb–Zn Deposits of Huayuan Ore-Concentrated District, Northwest Hunan Province, China. *Earth Sci.* **2018**, *43*, 2449–2464. (In Chinese)
18.　Xu, L.; Luo, C.G.; Wen, H.J.; Zhou, Z.B.; de Fourestier, J. The role of fluid mixing in the formation of vein-type Zn-Pb deposits in eastern Guizhou Province, SW China: Insights from elemental compositions and chlorine isotopes of fluid inclusions. *J. Asian Earth Sci.* **2022**, *239*, 105403. [CrossRef]
19.　Xia, X.J.; Fu, S.Y. Mineralization Pattern of North Western Hunan Lead-zinc Mine. *Nonferrous Met.* **2010**, *62*, 35–38. (In Chinese)
20.　Wei, H.T.; Shao, Y.J.; Xiong, Y.Q.; Liu, W.; Kong, H.; Li, Q.; Sui, Z.H. Metallogenic model of Huayuan Pb–Zn ore field in the western Hunan Province, South China. *J. Cent. South Univ.* **2017**, *48*, 2402–2413. (In Chinese)
21.　Zhou, J.X.; An, Y.L.; Yang, Z.M.; Luo, K.; Sun, G.T. New discovery of extraordinary enrichment of selenium in Dingtoushan Pb–Zn deposit, Qinglong City, Guizhou Province, and its geological significance. *Miner. Depos.* **2020**, *39*, 568–578. (In Chinese)
22.　Li, Z.F. A Preliminary Discussion on the Origin of Pb–Zn Ore Deposits in Western Hunan and Eastern Guizhou. *Guizhou Geol.* **1991**, *8*, 363–371. (In Chinese)
23.　Li, K.; Wu, C.X.; Tang, C.Y.; Duan, Q.F.; Yu, Y.S. Carbon and oxygen isotopes of Pb–Zn ore deposits in western Hunan and eastern Guizhou provinces and their implications for the ore-forming process. *Geol. China* **2014**, *41*, 1608–1619. (In Chinese)
24.　Wei, H.T.; Shao, Y.J.; Ye, Z.; Zhou, H.D. Geochemical characteristics of trace elements of sphalerite from Huayuan Pb–Zn ore field, western Hunan, China. *J. Chengdu Univ. Technol.* **2021**, *48*, 142–153. (In Chinese)
25.　Yang, D.Z.; Zhou, J.X.; Luo, K.; Yu, J.; Zhou, Z.H. New discovery and research value of Zhulingou zinc deposit in Guiding, Guizhou. *Bull. Mineral. Petrol. Geochem.* **2020**, *39*, 344–345. (In Chinese)
26.　Zhou, J.X.; Meng, Q.T.; Ren, H.Z.; Sun, G.T.; Zhang, Z.J.; An, Q.; Zhou, C.X. Discovery of super large paragenetic (associated) germanium deposit in Huangsi anticline, Guizhou. *Geotecton. Metallog.* **2020**, *44*, 1025–1026. (In Chinese)

27. Zhou, J.X.; Yang, D.Z.; Yu, J.; Luo, K.; Zhou, Z.H. Ge extremely enriched in the Zhulingou Zn deposit, Guiding City, Guizhou Province, China. *Geol. China* **2021**, *48*, 665–666. (In Chinese)

28. Zhou, J.X.; Luo, K.; Sun, G.T. Se extremely enriched in the Dingtoushan Pb–Zn deposit, Qinglong City, Guizhou Province, China. *Geol. China* **2021**, *48*, 339–340. (In Chinese)

29. Zhou, J.X.; Yang, D.Z.; Xiao, S.; An, Y.L.; Luo, K. Discovery and Significance of Thallium Supernormal Enrichment in Huodehong Lead—Zinc Deposit, Northeastern Yunnan. *Geotecton. Metallog.* **2021**, *45*, 427–429. (In Chinese)

30. Meng, Q.T.; Zhou, J.X.; Sun, G.T.; Zhao, Z.; An, Q.; Yang, X.Y.; Lu, M.D.; Xiao, K.; Xu, L. Geochemical characteristics and ore prospecting progress of the Banbianjie Zn deposit in Guiding City, Guizhou Province, China. *Acta Mineral. Sin.* **2021**, *23*, 616–619. (In Chinese)

31. Tu, G.Z.; Gao, Z.M.; Hu, R.Z.; Zhang, Q.; Li, C.Y.; Zhao, Z.H.; Zhang, B.G. *Dispersed Element Geochemistry and Mineralization Mechanism*; Geological Publishing House: Beijing, China, 2004; 421p. (In Chinese)

32. Zhai, M.G.; Wu, F.Y.; Hu, R.Z.; Jiang, S.Y.; Li, W.C.; Wang, R.C.; Wang, D.H.; Qi, T.; Qin, K.Z.; Wen, H.J. Critical metal mineral resources: Current research status and scientific issues. *Bull. Natl. Nat. Sci. Found. China* **2019**, *33*, 106–111. (In Chinese)

33. Wen, H.J.; Zhou, Z.B.; Zhu, C.W.; Luo, C.G.; Wang, D.Z.; Du, S.J.; Li, X.F.; Chen, M.H.; Li, H.Y. Critical scientific issues of super-enrichment of dispersed metals. *Acta Petrol. Sin.* **2019**, *35*, 3271–3291. (In Chinese)

34. Li, K.X.; Leng, C.B.; Ren, Z.; Liu, F.; Xu, D.R.; Ye, L.; Luo, T.Y. Progresses of researches on the dispersed elements associated with lead-zinc deposits. *Acta Mineral. Sin.* **2021**, *41*, 225–233. (In Chinese)

35. Hu, R.Z.; Su, W.C.; Qi, H.W.; Bi, X.W. Geochemistry, Occurrence and Mineralization of Germanium. *Bull. Mineral. Petrol. Geochem.* **2000**, *19*, 215–217. (In Chinese)

36. Zhang, Q.; Liu, Y.P.; Ye, L.; Shao, S.X. Study on Specialization of Dispersed Element Mineralization. *Bull. Mineral. Petrol. Geochem.* **2008**, *27*, 247–253. (In Chinese)

37. Wang, D.H.; Wang, R.J.; Li, J.K.; Zhao, Z.; Yu, Y.; Dai, J.J.; Chen, Z.H.; Li, D.X.; Qu, W.J.; Deng, M.C.; et al. The progress in the strategic research and survey of rare earth, rare metal and rare-scattered elements mineral resources. *Geol. China* **2013**, *40*, 361–370. (In Chinese)

38. Tao, Y.; Hu, R.Z.; Tang, Y.Y.; Ye, L.; Qi, H.W.; Fan, H.F. Types of dispersed elements bearing ore-deposits and their enrichment regularity in Southwest China. *Acta Geol. Sin.* **2019**, *93*, 1210–1230. (In Chinese)

39. Mao, J.W.; Yang, Z.X.; Xie, G.Q.; Yuan, S.D.; Zhou, Z.H. Critical minerals: International trends and thinking. *Miner. Depos.* **2019**, *38*, 689–698. (In Chinese)

40. Schwartz, M. Cadmium in zinc deposits: Economic geology of a polluting element. *Int. Geol. Rev.* **2000**, *42*, 445–469. [CrossRef]

41. Xue, C.J.; Chen, Y.C.; Yang, J.M.; Wang, D.H.; Yang, W.G.; Yang, Q.B. Jinding Pb–Zn Deposit: Geology and Geochemistry. *Miner. Depos.* **2002**, *21*, 270–277. (In Chinese)

42. Bradley, D.C.; Leach, D.L.; Symons, D.; Emsbo, P.; Premo, W.; Breit, G.; Sangster, D.F. Reply to discussion on "Tectonic controls of Mississippi Valley-type lead-zinc mineralization in orogenic forelands" by Kesler, S.E.; Christensen, J.T.; Hagni, R.D.; Heijlen, W.; Kyle, J.R.; Misra, K.C.; Muchez, P.; van derVoo, R, Mineralium Deposita. *Miner. Depos.* **2004**, *39*, 515–519. [CrossRef]

43. Si, R.J.; Gu, X.X.; Pang, X.C.; Fu, S.H.; Li, F.Y.; Zhang, M.; Li, Y.H.; Li, X.Y.; Li, J. Geochemical Character of Dispersed Element in Sphalerite from Fule Pb–Zn Polymetal Deposit, Yunnan Province. *Mineral. Petrol.* **2006**, *26*, 75–80. (In Chinese)

44. Zhou, J.X.; Huang, Z.L.; Zhou, G.F.; Li, X.B.; Ding, W.; Gu, J. The Occurrence States and Regularities of Dispersed Elements in Tianqiao Pb–Zn Ore Deposit, Guizhou Province, China. *Acta Mineral. Sin.* **2009**, *29*, 471–480. (In Chinese)

45. Zhou, J.X.; Huang, Z.L.; Zhou, M.F.; Li, X.B.; Jin, Z.G. Constraints of C-O-S-Pb isotope compositions and Rb-Sr isotopic age on the origin of the Tianqiao carbonate-hosted Pb–Zn deposit, SW China. *Ore Geol. Rev.* **2013**, *53*, 77–92. [CrossRef]

46. Hu, R.Z.; Chen, W.T.; Xu, D.R.; Zhou, M.F. Reviews and new metallogenic models of mineral deposits in South China: An introduction. *J. Asian Earth Sci.* **2017**, *137*, 1–8. [CrossRef]

47. Mandelbrot, B.B. Stochastic Models for the Earth's relief, the shape and the fractal dimension of the coastlines, and the number-area rule for islands. *Proc. Natl. Acad. Sci.* **1975**, *72*, 3825–3828. [CrossRef]

48. Zhang, J.; Wang, D.H.; Sun, B.S.; Chen, Z.H. Metallogenic Spatial Analysis Based on Fractal Theory: A Case Study of the Kangguertage Gold Ore Belt in Xinjiang. *Acta Geosci. Sinica.* **2009**, *30*, 58–64. (In Chinese)

49. Tan, K.X.; Hao, X.C.; Dai, T.G. Fractal Features of Fractures in China and Their Implication for Geotectonics. *Geotecton. Et Metallog.* **1998**, *22*, 17–20. (In Chinese)

50. Hu, X.Q.; Shi, Z.J.; Tian, Y.M.; Wang, C.C.; Cao, J.F. Multifractal feature and significance of Maokou Formation faults in the southeast of Sichuan. *J. Chengdu Univ. Technol.* **2014**, *41*, 476–482. (In Chinese)

51. Li, F.; Liu, G.S.; Zhou, Q.W.; Zhao, G.B. Application of fractal theory in the study of the relationship between fracture and mineral. *J. Hefei Univ. Technol.* **2016**, *39*, 701–706. (In Chinese)

52. Sun, T.; Li, H.; Wu, K.X.; Chen, L.K.; Liu, W.M.; Hu, Z.J. Fractal and Multifractal Characteristics of Regional Fractures in Tongling Metallogenic Area. *Nonferrous Met. Eng.* **2018**, *8*, 111–115. (In Chinese)

53. Chen, P.; Peng, S.Y.; Wang, P.F.; Chen, X.X.; Yang, T.; Liu, Y.J. Fractal and multifractal characteristics of geological faults in coal mine area and their control on outburst. *Coal Sci. Technol.* **2019**, *47*, 42–52. (In Chinese)

54. Cui, Z.L.; Liu, X.Y.; Zhou, J.X. Fractal characteristics of faults and its geological significance in Sichuan-Yunnan-Guizhou Pb–Zn metallogenic province, China. *Glob. Geol.* **2021**, *40*, 75–92. (In Chinese)

55. Cui, Z.L.; Zhou, J.X.; Luo, K. Fractal structure analysis and application prospect of Xingguo-Ningdu fluorite metallogenic belt in southern Jiangxi, China. *J. Jilin Univ.* **2022**, *52*, 1–18. [CrossRef]

56. Tan, K.X.; Liu, S.S.; Xie, Y.S. Multifractal analysis of ore deposits distribution in Alty, Xinjiang, China. *Geotecton. Et Metallog.* **2000**, *24*, 333–341. (In Chinese)

57. Cui, Z.L.; Kong, D.K. Fractal characteristic and range of reconnaissance in Xiong'er mountain ore-concentrated area and its vicinity, Henan Province. *Ind. Miner. Process.* **2021**, *50*, 1–7. (In Chinese)

58. Han, X.B.; Li, J.B.; Feng, Z.H.; Zhang, S.Y.; Liang, J.C.; Long, J.P. Spatial Fractal Characteristics of Gold-Silver Deposits in the Western and Northern Yunkai Uplift. *J. Guilin Univ. Technol.* **2010**, *30*, 15–20. (In Chinese)

59. Shi, G.D.; Jin, B.L.; Chen, B. Fractal study on correlation between distribution of ore spots and main traces in Anhui. *J. Guilin Univ. Technol.* **2020**, *40*, 271–277. (In Chinese)

60. Mokhtari, Z.; Sadeghi, B. Geochemical anomaly definition using multifractal modeling, validated by geological field observations: Siah Jangal area, SE Iran. *Geochemistry* **2021**, *81*, 125774. [CrossRef]

61. Cheng, Q.M.; Agterberg, F.P.; Bonham-Carter, G.F. A spatial analysis method for geochemical anomaly separation. *J. Geochem. Explor.* **1996**, *56*, 183–195. [CrossRef]

62. Parsa, M.; Sadeghi, M.; Grunsky, E. Innovative methods applied to processing and interpreting geochemical data. *J. Geochem. Explor.* **2022**, *237*, 106983. [CrossRef]

63. Xie, S.Y.; Bao, Z.Y. Application of multifractal to ore-forming potential evaluation. *J. Chengdu Univ. Technol.* **2004**, *31*, 28–33. (In Chinese)

64. Xie, S.; Cheng, Q.; Zhang, S.; Huang, K. Assessing microstructures of pyrrhotites in basalts by multifractal analysis. *Nonlinear Process. Geophys.* **2010**, *17*, 319–327. [CrossRef]

65. Zuo, R.G. Identifying geochemical anomalies associated with Cu and Pb–Zn skarn mineralization using principal component analysis and spectrum-area fractal modeling in the Gangdese Belt, Tibet (China). *J. Geochem. Explor.* **2011**, *111*, 13–22. [CrossRef]

66. Sun, X.; Zheng, Y.Y.; Wang, C.M.; Zhao, Z.Y.; Geng, X.B. Identifying geochemical anomalies associated with Sb-Au-Pb–Zn-Ag mineralization in North Himalaya, southern Tibet. *Ore Geol. Rev.* **2016**, *73*, 1–12. [CrossRef]

67. Zuo, R.G.; Wang, J. Fractal/multifractal modeling of geochemical data: A review. *J. Geochem. Explor.* **2016**, *164*, 33–41. [CrossRef]

68. Zhao, M.Y.; Xia, Q.L.; Wu, L.R.; Liang, Y.Q. Identification of multi-element geochemical anomalies for Cu–polymetallic deposits through staged factor analysis, improved fractal density and expected value function. *Nat. Resour. Res.* **2022**, *31*, 1867–1887. [CrossRef]

69. Lyu, C.; Cheng, Q.M.; Zuo, R.G.; Wang, W.P. Mapping Spatial Distribution Characteristics of Lineaments Extracted from Remote Sensing Image Using Fractal and Multifractal Models. *J. Earth Sci.* **2017**, *28*, 507–515. [CrossRef]

70. Cheng, Q.M. What are Mathematical Geosciences and its frontiers? *Earth Sci. Front.* **2021**, *28*, 6–25. (In Chinese)

71. Yin, F.G.; Xu, X.S.; Wan, F.; Chen, M. Characteristic of Seqence and Stratigraphical Division in Evolution of Upper Yangtze Region During Caledonian. *J. Stratigr.* **2002**, *26*, 315–319. (In Chinese)

72. Shu, L.S.; Zhou, X.M.; Deng, P.; Wang, B.; Jiang, S.Y.; Yu, J.H.; Zhao, X.X. Mesozoic tectonic evolution of the southeast China block: New insights from basin analysis. *J. Asian Earth Sci.* **2009**, *34*, 376–391. [CrossRef]

73. Yan, D.P.; Qiu, L.; Chen, F.; Li, L.; Zhao, L.; Yang, W.X.; Zhang, Y.X. Structural style and kinematics of the Mesozoic Xuefengshan intraplate orogenic belt. *Earth Sci. Front.* **2018**, *25*, 1–13. (In Chinese)

74. Cello, G. Fractal analysis of a Quaternary fault array in the central Apennines, Italy. *J. Struct. Geol.* **1997**, *19*, 945–953. [CrossRef]

75. Wang, W.; Liu, M.Y.; Shi, G.W.; Li, J.Q.; Wang, Y.Q. Fractal characteristics study of fractures in Zhaxikang ore-concentrated area of Longzi County, Tibet. *Geol. Miner. Resour. South China* **2016**, *32*, 358–365. (In Chinese)

76. Wu, C.J. Fractal characteristics of lineament in Fozichong lead-zinc district. *China Min. Mag.* **2017**, *26*, 233–236. (In Chinese)

77. Kruhl, J.H. *Fractals and Dynamic Systems in Geoscience*; Spring: New York, NY, USA, 1994; 421p.

78. Dong, F.Q. Fractal Characteristics of Fractures and Its Geological Significance in Gudui-Longzi Region in Southern Tibet. *Gold Sci. Technol.* **2012**, *20*, 41–45. (In Chinese)

79. Ding, S.J.; Zhai, Y.S. Fractal Study of Structural Traces in Jiaojia Gold Deposit, Jiaodong, China. *Earth Sci.* **2000**, *25*, 416–420. (In Chinese)

80. Zhou, Q.Y.; Tan, K.X.; Xie, Y.S. Fractal Character of Structural Control on Uranium Mineralization in South China. *J. Univ. South China* **2009**, *23*, 32–36. (In Chinese)

81. Xie, Y.S.; Yin, J.W.; Tan, K.X.; Tang, Z.P.; Duan, X.Z.; Hu, Y.; Wang, Z.Q.; Li, C.G.; Wang, Z.Z.; Feng, Z.G. Tectono-Magmatic Activization and Fractal Dynamics of Hydrothermal Uranium Ore Formation in South. *Geotecton. Metallog.* **2015**, *39*, 510–519. (In Chinese)

82. Lu, X.W.; Ma, D.S. Fractal dimensions of fracture systems in antimony metallogenic zones of central Hunan and their indicating significance for migration of ore forming fluids and location of ore deposits. *Miner. Depos.* **1999**, *18*, 168–174. (In Chinese)

83. Han, X.B.; Liang, J.C.; Feng, Z.H.; Zhang, G.L.; Chen, M.H. Fractal Features of Fractures and Their Relation to Silver-Gold Mineralization in Southeast Guangxi. *Guangxi Sci.* **2003**, *10*, 117–121. (In Chinese)

84. Wang, N.; Liu, Y.S.; Peng, N.; Wu, C.L.; Liu, N.Q.; Nie, B.F.; Yang, X.Y. Fractal characteristics of fault structures and their use for mapping ore-prospecting potential in the Qitianling area, southern Hunan province, China. *Acta Geol. Sin.* **2015**, *89*, 121–132.

85. He, H.; An, L.; Liu, W.; Yang, X.; Gao, Y.; Yang, L. Fractal characteristics of fault systems and their geological significance in the Hutouya poly-metallic ore field of Qimantage, east Kunlun, China. *Geol. J.* **2017**, *52*, 419–424. [CrossRef]

86. Mao, Z.L.; Peng, S.L.; Lai, J.Q.; Wang, L. Fractal studies of fracture and metallogenic prediction in the east area of Gejiu ore district. *Contrib. Geol. Miner. Resour. Res.* **2004**, *19*, 17–19. (In Chinese)

87. Sun, T.; Liao, Z.Z.; Wu, K.X.; Chen, L.K.; Liu, W.M.; Yi, C.Y. Fractal distribution characteristics and geological significances of fracture structure in Southern Jiangxi. *J. Jiangxi Univ. Sci. Technol.* **2017**, *38*, 48–54. (In Chinese)

88. Zhao, J.L.; Li, J.; Zhang, Z.; Yang, C.C.; Zhang, X.J. Multifractal characteristics of spatial distribution of the faults in west subsag of Bozhong Sag. *Oil Drill. Prod. Technol.* **2018**, *40*, 14–16. (In Chinese)

89. Shi, Z.J.; Luo, Z.T.; Peng, D.J.; He, Z.H. Multifractal characteristics of fault spatial distribution in Sichuan area. *Geoscience* **1995**, *9*, 467–474. (In Chinese)

90. Liao, J.F.; Feng, Z.H.; Luo, C.Q.; Kang, Z.Q. Fractal characteristics analysis of fractures in Shuiyanba ore field of Hezhou, Guangxi. *Miner. Depos.* **2012**, *31*, 459–464. (In Chinese)

91. Cui, Z.L.; Yao, Y.L.; Cheng, J.H.; Luo, K.; Zhou, J.X. Structural Fractal Texture Characteristics and Its Prospecting Significance for the Yadu-Mangdong Metallogenic Belt in NW Guizhou Province. *Geol. J. China Univ.* **2022**, *28*, 592–605. (In Chinese)

92. Lovejoy, S.; Schertzer, D. Multifractals, universality classes, and satellite and radar measurements of cloud and rain fields. *J. Geophys Res.* **1990**, *95*, 2021–2034. [CrossRef]

93. Stanley, H.E.; Meakin, P. Multifractal phenomena in physics and chemistry. *Nature* **1998**, *335*, 405–409. [CrossRef]

94. Cheng, Q.M.; Zhang, S.Y.; Zuo, R.G.; Chen, Z.J.; Xie, S.Y.; Xia, Q.L.; Xu, D.Y.; Yao, L.Q. Progress of multifractal filtering techniques and their applications in geochemical information extraction. *Earth Sci. Front.* **2009**, *16*, 158–198. (In Chinese)

95. Halsey, T.C.; Jensen, M.H.; Kadanoff, L.P.; Procaccia, I.I.; Shraiman, B.I. Fractal measures and their sing ularities, the characterization of strange sets. *Phys. Rev.* **1986**, *33*, 1141–1151. [CrossRef] [PubMed]

96. Cheng, Q. Multifractality and spatial statistics. *Comput. Geosci.* **1999**, *25*, 949–962. [CrossRef]

97. Xie, S.Y.; Bao, Z.Y. The Method of Moments and Its Application to The Study of Mineralization in Shaoguan District, North Guangdong, China. *J. Chang. Univ. Sci. Technol.* **2003**, *33*, 443–448. (In Chinese)

98. Grau, J.; Méndez, V.; Tarquis, A.M.; Díaz, M.C.; Saa, A. Comparison of gliding box and box-counting methods in soli image analysis. *Geoderma* **2006**, *134*, 349–359. [CrossRef]

99. Zhou, G.Z.; Wang, C.Z.; Liu, Y.Z.; Xiao, T.F. Application of Multifractal Theory in the Environmental Sciences. *Bull. Mineral. Petrol. Geochem.* **2013**, *33*, 107–113. (In Chinese)

100. Cao, H.Q.; Zhu, G.X.; Li, X.T.; Xia, W.F. Multi-fractal and its application in terrain character analysis. *J. Beijing Univ. Aeronaut. Astronaut.* **2004**, *30*, 1182–1185. (In Chinese)

101. Wen, H.M.; Xiao, C.X.; Li, R.; Yang, B.; Wang, H. On Multifractal Analysis Method in Well Logging Interpretation. *Well Logging Technol.* **2004**, *28*, 381–385. (In Chinese)

102. Wang, W.G. *Software System Design of Geochemical Data Processing—Fractal Volume*; China University of Geosciences: Beijing, China, 2006; 64p. (In Chinese)

103. Liu, X.M. *Fractal Software System Used in Tungsten Forecast of Dajishan*; China University of Geosciences: Beijing, China, 2009; 66p. (In Chinese)

104. Shi, J.F.; Wang, C.N. Fractal analysis of gold deposits in China: Implication for giant deposit exploration. *Earth Sci.* **1998**, *23*, 616–619. (In Chinese)

105. Li, C.J.; Jiang, X.L.; Xu, Y.L.; Ma, T.H. Fractal Study of Mesozoic Hydrothermal Deposits in Zhejiang Province. *Chin. J. Geol.* **1996**, *31*, 55–64. (In Chinese)

106. Li, C.J.; Ma, T.H.; Zhu, X.S. *Fractal, Chaos and ANN in Mineral Exploration*; Geological Publishing House: Beijing, China, 1999; 140p. (In Chinese)

107. Fry, H. Random point distributions and strain measurement in rocks. *Tecomophysics* **1979**, *60*, 89–105. [CrossRef]

108. Stone, D.; Schwerdtner, W.M. Total strain within a major mylonite zone, southern Canadian Shield. *J. Struct. Geol.* **1981**, *3*, 193–194.

109. Ramsay, J.G.; Huber, M.I. *The Techniques of Modern Structural Geology, Volume 1: Strain Analysis*; Academic Press: London, UK, 1983.

110. Lacassin, R.; Driessche, J. Finite strain determination of gneiss: Application of Fry's method to porphyroid in the southern Massif Central (France). *J. Struct. Geol.* **1983**, *5*, 245–253. [CrossRef]

111. Vearncombe, J.; Vearncombe, S. The spatial distribution of mineralization: Applications of Fry analysis. *Econ. Geol.* **1999**, *94*, 475–486. [CrossRef]

112. Austin, J.R.; Blenkinsop, T.G. Local to regional scale structural controls on mineralisation and the importance of a major lineament in the eastern Mount Isa Inlier, Australia: Review and analysis with autocorrelation and weights of evidence. *Ore Geol. Rev.* **2009**, *35*, 298–316. [CrossRef]

113. Parsa, M.; Maghoudi, A.; Yousefi, M. Spatial analyses of exploration evidence data to model skarn-type copper prospectivity in the Varzaghan district, NW Iran. *Ore Geol. Rev.* **2018**, *92*, 97–112. [CrossRef]